small methods
www.small-methods.com

Recent Advances and Perspective on Electrochemical Ammonia Synthesis under Ambient Conditions

Yang Li, Qi Zhang, Zongwei Mei, Shunning Li, Wenbin Luo, Feng Pan,* Huakun Liu, and Shixue Dou**

Ammonia is an essential chemical for agriculture and industry. To date, NH_3 is mainly supplied by the traditional Haber–Bosch process, which is operated under high-temperature and high-pressure in a centralized way. To achieve ammonia production in an environmentally benign way, electrochemical NH_3 synthesis under ambient conditions has become the frontier of energy and chemical conversion schemes, as it can be powered by renewable energy and operates in a decentralized way. The recent progress on developing different strategies for NH_3 production, including 1) classic NH_3 synthesis pathways over nanomaterials; 2) the Mars-van Krevelen (MvK) mechanism over metal nitrides (MN_x); 3) reducing the nitrate into NH_3 over Cu-based nanomaterial; and 4) metal–N_2 battery release of NH_3 from Li_xM. Moreover, the most recent advances in engineering strategies for developing highly active materials and the design of the reaction systems for NH_3 synthesis are covered.

1. Introduction

Owing to its essential role in producing fertilizer, chemicals, and pharmaceutical products, ammonia (NH_3) synthesis is considered as one of the foundational chemical industries that promotes the development of human society.[1,2] The industrial product NH_3 has also received much more attention as an alternative energy carrier to realize the zero-carbon concept due to its large hydrogen capacity (17.6 wt%) and high energy density (4.3 kWh h^{-1}).[3] The invention of the Haber–Bosch (H–B) process in the 20th century had an enormous impact on human society when it achieved the artificial synthesis of ammonia at the high reaction temperature of ≈500 °C and high pressure of 200–300 atm.[4,5] During this process, however, 1%–2% of the world annual energy output is consumed and two times the amount of greenhouse gas is released for each ton of NH_3.[6–8] Therefore, it is imperative to explore and develop a sustainable way to produce NH_3 under mild conditions, ideally at low temperature and pressure.

In nature, the global nitrogen (N_2) cycle, from N_2 to NH_3, primarily relies on biological N_2 fixation by nitrogenase enzymes under ambient conditions through multiple proton and electron transfer steps.[9–13] Inspired by this catalytic mechanism, the electrochemical synthesis of NH_3 can offer a promising environmentally friendly process for sustainable artificial yield of NH_3 at room temperature and pressure, using protons and electrons powered by renewable energy from solar or wind sources.[14–17] Ultimately, the electrochemical nitrogen reduction reaction (NRR) directly from N_2 and H_2O has been regarded as an optimal route since the 1960s.[18–23] Due to the successful strategy of combining theoretical and experimental studies, the field of NRR has obtained important breakthroughs in the past few years in the development of highly efficient catalysts, which have notably improved the Faradaic efficiency (FE) from <1% to >10%.[24–32]

To date, various strategies have been developed to design nanomaterials for further improving the NRR performance, including heteroatom dopants,[33–35] interface engineering,[36] alloys,[37,38] facet engineering,[39,40] defects,[41–43] and the size effect[44–49] coupled with an optimized electrochemical reaction system. However, because the competing hydrogen evolution reaction (HER) and the by-product N_2H_4 formation, there is still a big gap facing N_2 fixation before it can move into future practical application, such as low FE and low yield rate. Excitingly, recent advances have addressed the problems of the low solubility of N_2 and of circumventing the HER. The metal nitride (MN_x) and nitrates substitute for N_2 as the nitrogen source, which can effectively improve the NH_3 synthesis efficiency.[50–52] Simultaneously, converting nitrate (NO_3^-) contamination to NH_3 and metal–N_2 battery have become promising alternative strategies for electrochemical NH_3 synthesis.[53–60]

In this review, we summarize recently advanced strategies for the electrochemical synthesis of NH_3 under ambient conditions (**Figure 1**) to inspire new thoughts, revisits, and ultimately, innovations in this field. The fundamentals of various electrochemical NH_3 synthesis pathways, including the reaction mechanisms

Y. Li, Q. Zhang, W. Luo, H. Liu, S. Dou
Institute for Superconducting and Electronic Materials
University of Wollongong
Wollongong, NSW 2522, Australia
E-mail: luow@uow.edu.au; shi@uow.edu.au
Y. Li, Z. Mei, S. Li, F. Pan
School of Advanced Materials
Peking University
Shenzhen Graduate School
Shenzhen 518055, P. R. China
E-mail: panfeng@pkusz.edu.cn

The ORCID identification number(s) for the author(s) of this article can be found under https://doi.org/10.1002/smtd.202100460.

DOI: 10.1002/smtd.202100460

 © 2021 Wiley-VCH GmbH

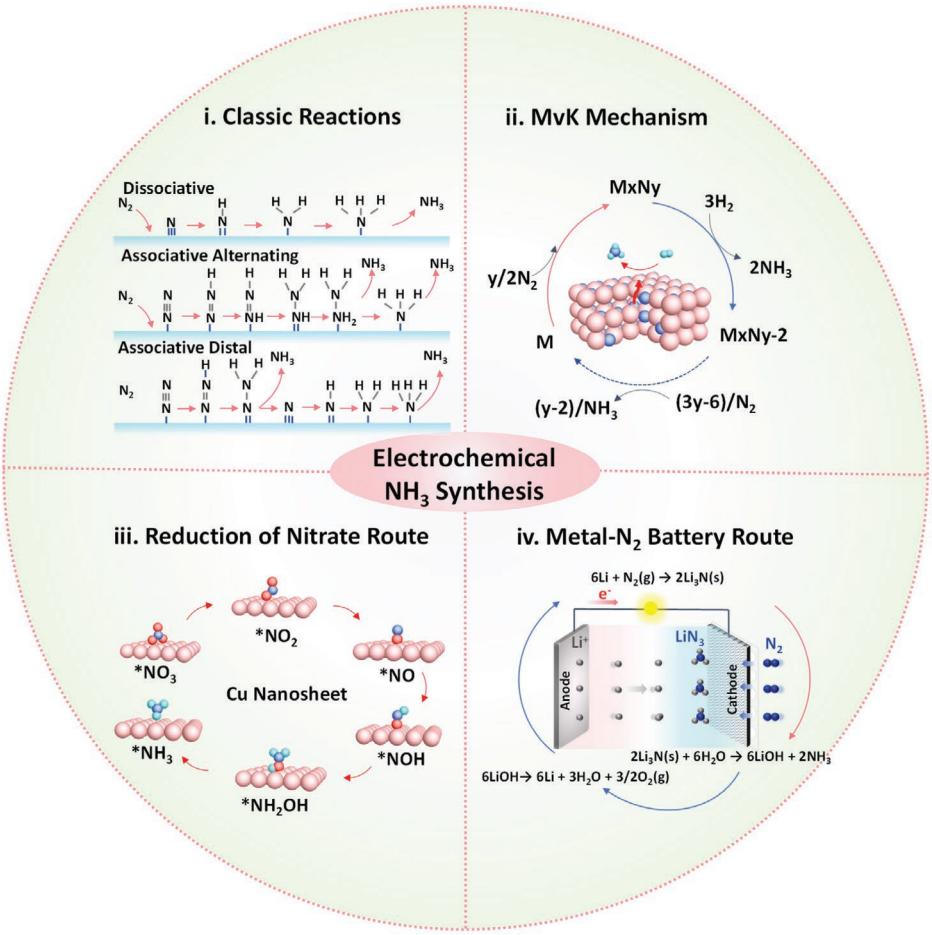

Figure 1. Overview of electrochemical NH_3 synthesis via four kinds of reaction routes. i) Classic mechanism for electrochemical nitrogen reduction. ii) MvK mechanism over metal nitride. iii) Reduction of nitrate over a Cu-based material. iv) Li–N_2 battery release of NH_3 from Li_3N.

are first introduced. Then, we comprehensively discuss the advanced strategies in material design, based on the combination of theoretical calculations and experimental investigations to spur more fundamental mechanistic investigations. In addition to the materials, the choice of electrolyte and the reaction cell are also succinctly discussed, with the aim of promoting our understanding of the electrochemical reaction system and stimulating further experimental improvements. Lastly, we present the critical challenges, possible solutions, and future perspectives on the research on electrochemical NH_3 production. Through this review, we hope to systematically present the readers with the latest advances in this field, and more importantly, shed light on the future development of materials, systems, and strategies for the electrochemical synthesis of ammonia.

2. Fundamentals of Electrochemical NH_3 Synthesis

2.1. Reaction Routes

2.1.1. Classic Reaction Mechanism

Biological reduction of N_2 to NH_3 can occur on the FeMo protein of nitrogenases under ambient conditions as follows

$$N_2 + 8H^+ + 8e^- + 16ATP \rightarrow 2NH_3 + H_2 + 16ADP + 16Pi \quad (1)$$

Inspired by this mechanism, various electrocatalysts were designed and the corresponding mechanism was explored.[61–64] Generally, associative and dissociative mechanisms are possible for this catalysis process, as shown in Figure 1i.[65,66] In the associative mechanism (including distal and alternating pathways, analogous to the mechanism in the enzyme) summarized in **Table 1** 1-1 to 1-8, the hydrogenation process from N_2 proceeds with its two N atoms bonded to each other. Such a hydrogenation process is further divided into two pathways, involving the distal pathway and the alternating pathway. In the distal pathway, the hydrogenation takes place preferentially on the N atom furthest away from the surface, leading to the release of the first ammonia molecule. The remaining N exists as M≡N, and the hydrogenation process is continued to produce the second ammonia. In the alternating pathway, the hydrogenation alternates between two N atoms, and the second NH_3 will be released just following the release of the first ammonia.

For instance, the reaction mechanism on flat or/and stepped Ru (0001) has been widely investigated through theoretical calculations.[67–69] Skúlason et al. explored the reaction pathways

© 2021 Wiley-VCH GmbH

23669608, 2021, 11, Downloaded from https://onlinelibrary.wiley.com/doi/10.1002/smtd.202100460 by University Town Of Shenzhen, Wiley Online Library on [26/11/2025]. See the Terms and Conditions (https://onlinelibrary.wiley.com/terms-and-conditions) on Wiley Online Library for rules of use; OA articles are governed by the applicable Creative Commons License

Table 1. Classic reaction mechanisms of the NRR.

Mechanism	Reaction	Step
Associative	$* + N_2 \rightarrow *N_2$	1-1
	$*N_2 + 6\,(H^+ + e^-) \rightarrow *N_2H + 5\,(H^+ + e^-)$	1-2
	$*N_2H + 5\,(H^+ + e^-) \rightarrow *NHNH + 4\,(H^+ + e^-)$	1-3a
	$*NHNH + 4\,(H^+ + e^-) \rightarrow *NHNH_2 + 3\,(H^+ + e^-)$	1-4a
	$*N_2H + 5\,(H^+ + e^-) \rightarrow *NNH_2 + 4\,(H^+ + e^-)$	1-3b
	$*NNH_2 + 4\,(H^+ + e^-) \rightarrow *N + NH_3 + 3\,(H^+ + e^-)$	1-4b
	$*N + 3\,(H^+ + e^-) \rightarrow *NH + 2\,(H^+ + e^-)$	1-5
	$*NH + 2\,(H^+ + e^-) \rightarrow *NH_2 + (H^+ + e^-)$	1-6
	$*NH_2 + (H^+ + e^-) \rightarrow *NH_3$	1-7
	$*NH_3 \rightarrow NH_3 + *$	1-8
Dissociative	$2* + N_2 \rightarrow 2*N$	1-9
	$2*N + 6\,(H^+ + e^-) \rightarrow *N + *NH + 5\,(H^+ + e^-)$	1-10
	$*N + *NH + 5\,(H^+ + e^-) \rightarrow 2*NH + 4\,(H^+ + e^-)$	1-11
	$2*NH + 4\,(H^+ + e^-) \rightarrow *NH + *NH_2 + 3\,(H^+ + e^-)$	1-12
	$*NH + *NH_2 + 3\,(H^+ + e^-) \rightarrow 2*NH_2 + 2\,(H^+ + e^-)$	1-13
	$2*NH_2 + 2\,(H^+ + e^-) \rightarrow *NH_2 + *NH_3 + (H^+ + e^-)$	1-14
	$*NH_2 + *NH_3 + H^+ + e^- \rightarrow 2*NH_3$	1-15
	$2*NH_3 \rightarrow *NH_3 + NH_3 + *$	1-16
	$*NH_3 + NH_3 + * \rightarrow 2NH_3 + 2*$	1-17

on the stepped Ru (0001) surface via associative mechanism (**Figure 2**a) and dissociative mechanism (Figure 2b). The density functional theory (DFT) calculations showed that the intact N_2 binds strongly on Ru (0001) with an adsorption energy of –0.4 eV. Due to the loss in entropy in transferring from the gas phase to the surface bound molecule, the free energy change is estimated to be +0.08 eV. The most exergonic step is the first hydrogenation step, 0.75 eV uphill in energy and 1.08 eV in free energy.[65]

Unlike the associative mechanism, in the dissociative mechanism, the cleavage of N≡N bonds takes place before hydrogenation, leaving a sole N adatom on the surface. Then the adsorbed N atoms are converted to NH_3 via a consecutive hydrogenation process (Table 1 1-9 to 1-17).

For an electrochemical NRR system, the ammonia formation only needs N_2, water, and electricity under ambient conditions. Furthermore, the N_2 and electricity can be conceivably supplied by the air and renewable energy, respectively, implying that the electrochemical system is potentially the most viable energy system to replace the H–B process. Generic equations for such an aqueous NRR system are described based on acid and basic conditions, as shown in **Table 2.**[70]

It is worth noting that, based on the thermodynamic principle, the first bond cleavage energy of N_2 amounts to 410 kJ mol^{-1}, and the first H addition to N_2 is endothermic (ΔH^0 = +36.6 kJ mol^{-1}), which increases the difficulty of protonation for N_2.[71] Furthermore, in aqueous electrolytes,

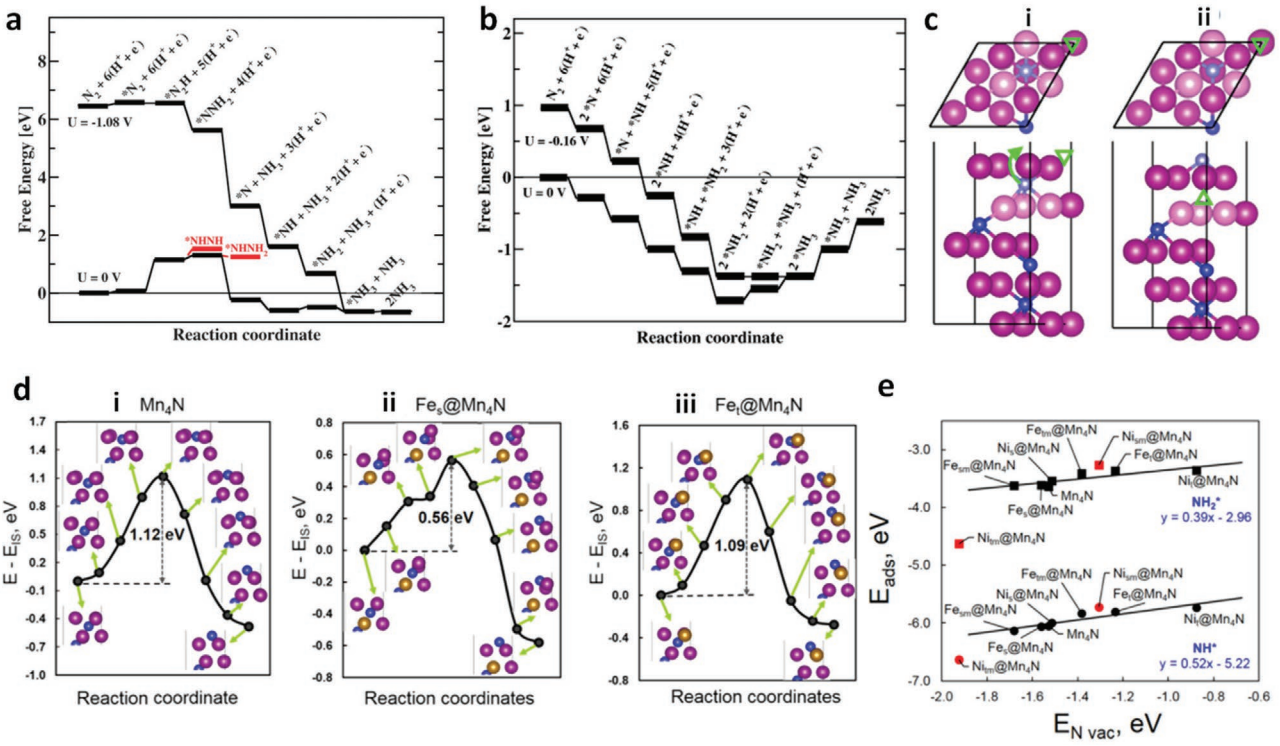

Figure 2. a) Energy profile on flat Ru (0001) via the associative mechanism with the applied electrode potential, $U = 0$ V and $U = -1.08$ V. b) Energy profile on flat Ru (0001) via the dissociative mechanism under $U = 0$ V and $U = -0.16$ V. Reproduced with permission.[65] Copyright 2012, The Royal Society of Chemistry. c) The diffusion of sublayer lattice N in i) the initial state and ii) the final state. d) The energy requirement for N diffusion from the sublayer to the surface for different materials: i) Mn_4N, ii) $Fe_s@Mn_4N$, and iii) $Fe_t@Mn_4N$. e) Scaling relationships between N binding energy ($E_{N\ vac}$) and the adsorption energies of NH* (circle) and NH_2* (square). Reproduced with permission.[73] Copyright 2018, American Chemical Society.

© 2021 Wiley-VCH GmbH

23669608, 2021, 11, Downloaded from https://onlinelibrary.wiley.com/doi/10.1002/smtd.202100460 by University Town Of Shenzhen, Wiley Online Library on [26/11/2025]. See the Terms and Conditions (https://onlinelibrary.wiley.com/terms-and-conditions) on Wiley Online Library for rules of use; OA articles are governed by the applicable Creative Commons License

Table 2. Classic reaction steps of the NRR in acidic and basic solutions. E^0: standard electrode potential of hydrogen; NHE: normal hydrogen electrode; SHE: standard hydrogen electrode.

Media	Electrode	Reaction	Step
Acidic	Anode	$3H_2O \rightarrow 3/2O_2$ (g) + $6H^+ + 6e^-$	2-1
	Cathode	$N_2 + 6H^+ + 6e^- \rightarrow 2\ NH_3$ (g), $E^0 = +0.55$ V vs NHE	2-2
	HER	$2H^+ + 2e^- \rightarrow H_2$ (g), $E^0 = 0$ V vs SHE at pH = 0	2-3
Basic	Anode	$OH^- \rightarrow 3H_2O + 3/2O_2 + 6e^-$	2-4
	Cathode	$N_2 + 6H_2O + 6e^- \rightarrow 2NH_3 + 6OH^-$, $E^0 = -0.736$ V vs SHE at pH = 14	2-5
	HER	$2H_2O$ (l) + $2e^- \rightarrow H_2$(g) + $2OH^-$, $E^0 = -0.828$ V vs SHE at pH = 14	2-6
Overall Reaction		$N_2 + 3H_2O \rightarrow 3/2O_2 + 2NH_3$	2-7

considering the equilibrium potential of the electrochemical NRR and HER, the HER will be the major side reaction during the NRR process.[66,72]

2.1.2. Mars-van Krevelen (MvK) Mechanism

Besides the associative mechanism and dissociative mechanism, an MvK mechanism was proposed for metal nitride (MN*x*) by Abghoui et al.[50–52] The details for this mechanism are illustrated in Figure 1ii. The NH_3 is produced by the lattice N, leading to lattice vacancies which will be further replenished with the gaseous N_2.[50,74,75] Moreover, the theoretical study of MN_x for the NRR also suggested that transition metal nitrides, such as VN and ZrN, can suppress the HER and achieve the NRR at low onset potentials.[50]

It is worth noting that heteroatom dopants may improve the NRR activity of metal nitrides. Li and co-workers reported that Fe-doping can remarkably decrease the energy cost from 1.75 eV (MoN_2) to 0.47 eV (Fe-doped MoN_2) and effectively improve the NRR performance.[76] Compared to the strong Mo–N interaction, the Fe can weaken the metal–N bonding, which is of benefit for N_2 activation and NH_3 formation, while the high spin state of four-coordinated Fe also contributes to the improvement of NRR performance. Similarly, Shan et al. also found that Fe and Ni doped MnN_4 can tune the electronic structure and lower the N diffusion energy barrier ($E_{a,vac}$).[73] While the binding energy of $H/NH_2/NH_3$ on Mn_4N is the performance-limiting factor, the sublayer lattice N diffusion barrier also play an important role in improving the NRR performance. The sublayer lattice N can diffuse onto the surface for continuous NRR reactions (Figure 2c). The DFT calculations revealed that, when Fe atoms are doped within sublayer ($Fe_s@Mn_4N$), the energy barrier ($E_{a\ vac}$) can be dramatically decreased from 1.12 to 0.56 eV. The Fe doped into top layer ($Fe_t@Mn_4N$), however, results in no obvious enhancement of N diffusion with $E_{a,vac}$ of 1.09 eV (Figure 2d). That is because when the Fe forms weaker bonds with nitrogen than those for Mn–N, the energy barrier of N is expected to be lower. Moreover, a series of Fe- and Ni-doped Mn_4N models were established, and the scaling relationships between the N binding energy ($E_{N\ vac}$) and the adsorption energies of NH* and NH_2* were further developed to evaluate the NH_3 energetic trends (Figure 2e).

2.1.3. Reduction of Nitrate into NH_3 Route

Nitrate electroreduction (NtrRR) has been regarded as an alternative route for the nitrogen reduction reaction, which can generate NH_3 using nitrate from industrial wastewater.[53–57,77] Cu-based nanomaterials have been extensively used in NtrRR and exhibited two orders of magnitude higher performance than the electrochemical NRR. Fu and co-workers have achieved a yield rate of 390.1 g mg_{Cu}^{-1} h^{-1} and a Faradaic efficiency of 99.7% using Cu nanosheets.[53]

Zhang's group also reported a high Faradaic efficiency of 97.0% for NtrRR using CuO nanowire arrays (NWAs).[36] As shown in **Figure 3**a, the Cu/Cu_2O NWAs can deliver higher current density with NO_3^- than without NO_3^-, indicating that the process involves electrocatalytic NO_3^- reduction to NH_3. When the reaction time was prolonged under −0.85 V, the concentration of NH_3 continued to increase, while the concentration of NO_3^- kept decreasing (Figure 3b). Both results demonstrate that the NO_3^- could be converted into NH_3. In situ Raman spectroscopy and ex situ experiments further reveal the electrochemical conversion from CuO to Cu/Cu_2O, which could serve as the active site due to the electron transfer at the interface of Cu/Cu_2O. Moreover, the DFT calculations further revealed that the Cu/Cu_2O possessed a higher energy barrier for the HER than that of Cu (Figure 3c), suggesting that Cu/Cu_2O could suppress the HER and enhance the selectivity and Faradaic efficiency of the NtrRR.

Apart from the typical Cu-based material serving as the NtrRR catalyst, there are also some other metal based catalysts, which can efficiently reduce the nitrate into NH_3, such as Ru,[78] Fe,[79] Ti.[80] Li et al. reported that Ru/oxygen-doped-Ru core/shell nanoclusters could prevent the HER and exhibit an NH_3 yield rate of 5.56 mol g_{cat}^{-1} h^{-1}.[78] The degree of strain of the Ru-based electrocatalyst was tailored by adjusting the subsurface oxygen concentration (Figure 3g,h). As shown in Figure 3d–f, the oxygen concentration of 6.3 at%, 2.9 at%, and 0.09 at% can trigger strain of 12% (Ru-ST-12), 5% (Ru-ST-5), and 0.6% (Ru-ST-0.6). The HER side reaction and NtrRR performance over the different strained Ru nanoclusters were summarized. As shown in Figure 3i, the higher strain Ru exhibited more pronounced HER inhibition and higher NtrRR performance, and the trend was followed of Ru-ST-12 > Ru-ST-5 > Ru-ST-0.6. The DFT calculations further revealed the underlying mechanism. Firstly, during the Heyrovsky reaction

© 2021 Wiley-VCH GmbH

23669608, 2021, 11, Downloaded from https://onlinelibrary.wiley.com/doi/10.1002/smtd.202100460 by University Town Of Shenzhen, Wiley Online Library on [26/11/2025]. See the Terms and Conditions (https://onlinelibrary.wiley.com/terms-and-conditions) on Wiley Online Library for rules of use; OA articles are governed by the applicable Creative Commons License

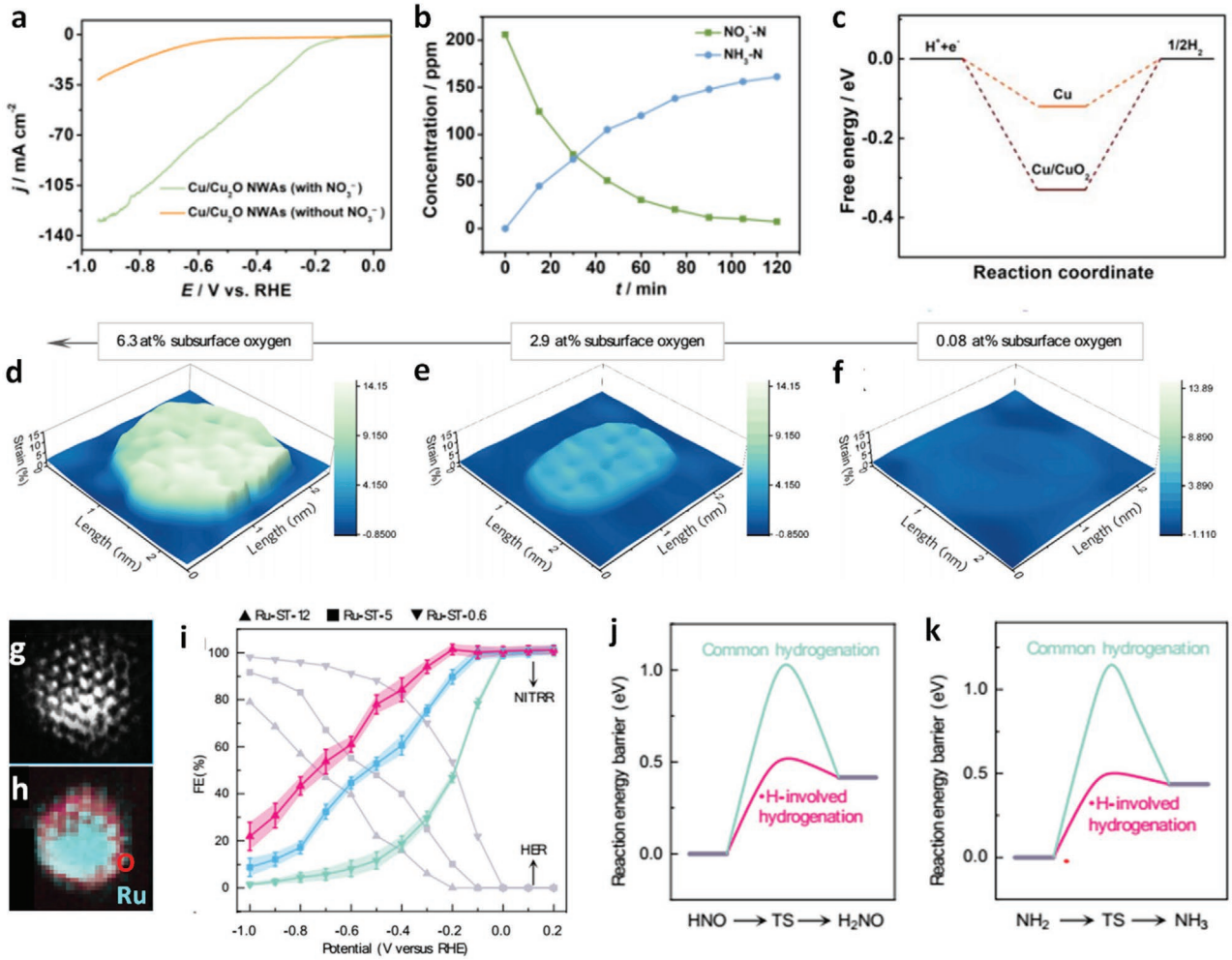

Figure 3. a) Linear sweep voltammetry (LSV) curves of Cu/Cu_2O NWAs with or without NO_3^-. b) The concentration changes of NO_3^- and NH_3 under −0.85 V. c) Free energy diagram for the HER over Cu and Cu/Cu_2O. Reproduced with permission.[36] Copyright 2020, Wiley-VCH. 3D topographic strain distribution images of d) Ru-ST-12, e) Ru-ST-5, and f) Ru-ST-0.6. g) HAADF–STEM images, and h) corresponding energy dispersive spectroscopy (EDS) mapping. i) FE_{NtrRR} and FE_{HER} of different strained Ru nanoclusters. The free energy diagram j) from HNO to H_2NO and k) from NH_2 to NH_3. Reproduced with permission.[78] Copyright 2020, American Chemical Society.

process for the HER, part of the adsorbed *H*, H_{ads}, could evolve into hydrogen radicals (•H) existing in the reaction medium. Secondly, the existence of •H could effectively reduce the transition state (TS) energies of HNO to H_2NO and NH_2 to NH_3 over the strained Ru by 1.09 and 1.26 eV to 0.53 and 0.51 eV (Figure 3j,k), respectively.

2.1.4. Metal–N_2 Battery

Metal–N_2 batteries have aroused widespread interest, for what is regarded as a "killing two birds with one stone" strategy. Metal–N_2 batteries not only storage/release energy, but also harness N_2 to produce valuable chemicals.[58,59,81] An electrochemical approach proposed for producing ammonia is electrochemical lithium cycling, which involves separate steps of LiOH electrolysis, direct nitridation of Li, and the release of NH_3 from Li_3N, thus circumventing the HER and achieving an initial current efficiency of 88.5%.[22]

Briefly, Li^+ ions are first reduced to Li metal in the absence of protons or N_2 available at potentials more negative than −3.3 V versus the standard hydrogen electrode (SHE). Next, the Li_3N is formed by adding the N_2 to the lithium via an energetically favorable and kinetically fast reaction. Finally, the Li_3N spontaneously breaks down to NH_3 and Li^+ under 0 V versus SHE when the protons are introduced (**Figure 4**a).[22] The three steps are listed in **Table 3**, including step 1: LiOH electrolysis, step 2: direct reaction of metallic Li with N_2 to form Li_3N, step 3: release of NH_3 by reaction with H_2O. The step 2 (conversion of Li to Li_3N) process was performed between 22 and 100 °C. As shown in Figure 4b, the initial conversion rate to Li_3N is increased with increasing temperature. When the time was prolonged to 12 h, the Li could be completely converted into nitride independently of temperature. The DFT calculations also suggested that other transition metals may further enhance the electrochemical ammonia production (Figure 4c).

Similarly, based on the reversible N_2/Li_3N reaction ($6Li + N_2 \rightarrow 2Li_3N$), Zhang et al. successfully designed a

© 2021 Wiley-VCH GmbH

23669608, 2021, 11, Downloaded from https://onlinelibrary.wiley.com/doi/10.1002/smtd.202100460 by University Town Of Shenzhen, Wiley Online Library on [26/11/2025]. See the Terms and Conditions (https://onlinelibrary.wiley.com/terms-and-conditions) on Wiley Online Library for rules of use; OA articles are governed by the applicable Creative Commons License

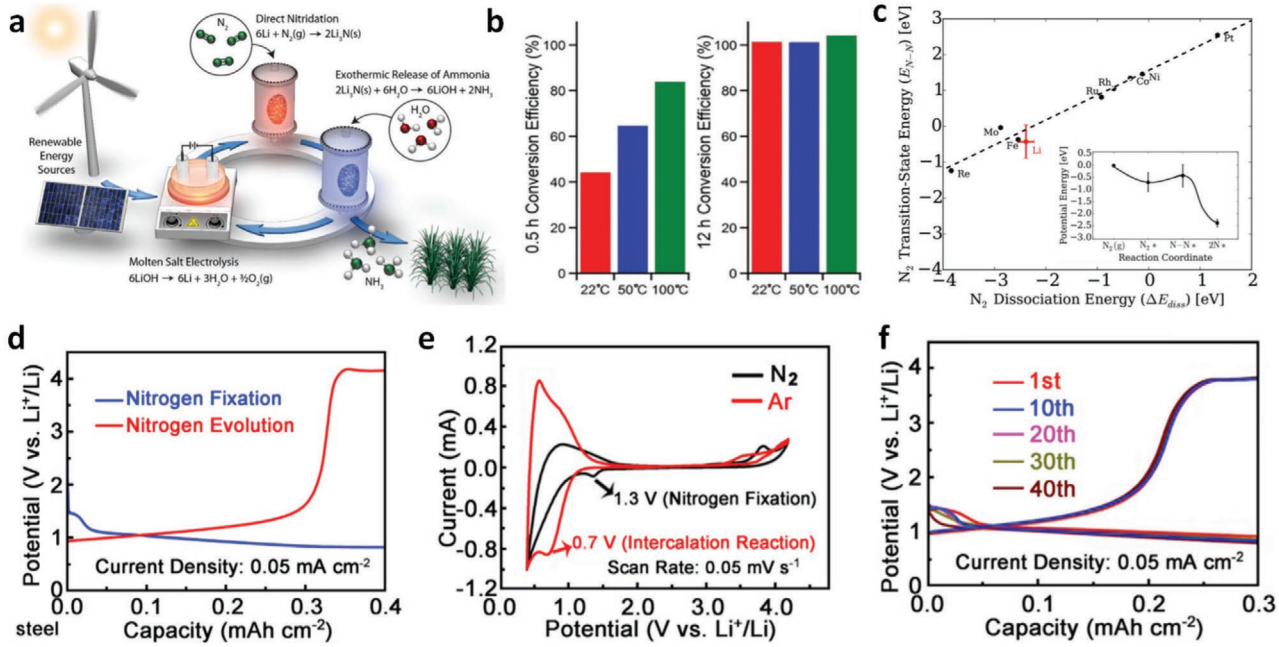

Figure 4. Synthesizing NH_3 via a Li-mediated cycling process. a) Illustration of ammonia synthesis by the Li-mediated cycling process. b) Ammonia conversion efficiency via the Li nitridation process under different conditions. Reproduced with permission.[22] Copyright 2017, The Royal Society of Chemistry. c) Scaling relationship between N_2 dissociation energy and N–N transition state energy on stepped transition metal surfaces (black) with the Li BCC (110) facet overlaid in red. d) Charging and discharging curve of the Li–N_2 battery at a current density of 0.05 mA cm^{-2}. e) Cyclic voltammetry (CV) curves of the Li–N_2 battery at a scan rate of 0.05 mV s^{-1} in Ar- and N_2-saturated atmospheres. f) Cycling performance of a Li–N_2 battery at a current density of 0.05 mA cm^{-2}. Reproduced with permission.[23] Copyright 2017, Elsevier Inc.

special Li–N_2 battery for N_2 fixation.[23] The Li–N_2 battery consisted of an Li-foil anode, a glass fiber separator, an ether-based electrolyte, and a carbon cloth (CC) cathode. For the discharging reactions, the injected N_2 molecules were first activated by accepting electrons from the cathode surface, and then combined with Li^+ to form the discharge product Li_3N. Next, the solid product Li_3N was decomposed into Li and N_2 in the charging process. The new pathway could achieve a FE of 59% and provide an efficient method for N_2 fixation. As shown in Figure 4d, the Li–N_2 battery exhibited the typical charging–discharging curve of the Li–N_2 battery. The CV curves measured under N_2-saturated atmosphere showed a typical cathodic peak at 1.3 V, which could be attributed to the N_2 fixation reaction (Figure 4e). The cycling performance is shown in Figure 4f, where the charge and discharge potentials underwent slight deviations after 40 cycles, which may have resulted from the instability of the cathode and anode. Besides the Li–N_2 battery, the Al–N_2 battery has recently been reported, which can generate power and yield NH_3 at a rate of 27.1 mg g_{cat}^{-1} h^{-1}.[82]

Table 3. The mechanism of the Li-mediated cycling process.

Step	Reaction
	$6Li^+ + 6e^- \rightarrow 6Li$ (Cathode)
Step 1	$6OH^- \rightarrow 3H_2O + 3/2O_2$ (g) + $6e^-$ (Anode)
	$6LiOH \rightarrow 6Li + 3H_2O + 3/2O_2$ (g) (Total Cell)
Step 2	$6Li + N_2$ (g) $\rightarrow 2Li_3N$(s)
Step 3	$2Li_3N(s) + 6H_2O \rightarrow 6LiOH + 2NH_3$

2.2. Modeling of Electrocatalytic Processes

For the complicated electrochemical NH_3 synthesis process, DFT calculations played a significant role in constructing the free energy diagram, establishing the reaction mechanism, and estimating volcano plots among the different catalysts.[83–85]

2.2.1. Gibbs Free Energy Landscape

During the electrochemical ammonia synthesis process, the reaction free energies (ΔG) of each element reaction were calculated according to the computational hydrogen electrode (CHE) model proposed by Norskov et al.[84] When the pH value was set zero, the free energy value can be obtained as follow

$$\Delta G = \Delta E + \Delta ZPE - T\Delta S + \Delta G_U \tag{2-8}$$

Where ΔE can be determined by DFT, ΔZPE is the zero point energy difference, and $T\Delta S$ is the change in entropy at 298.15 K. ΔG_U is the contribution of the electrode potential to ΔG at the applied electrode potential (U). The adsorption energy of N_2 and the intermediates can be defined as follows

$$\Delta E = E_T - E_{catalyst} - E_{adsorbate} \tag{2-9}$$

Where E_T, $E_{catalyst}$, and $E_{adsorbate}$ are the total energy of an adsorbed system, and the energies of an isolated catalyst and the gas-phase adsorbate, respectively.

© 2021 Wiley-VCH GmbH

23669608, 2021, 11, Downloaded from https://onlinelibrary.wiley.com/doi/10.1002/smtd.202100460 by University Town Of Shenzhen, Wiley Online Library on [26/11/2025]. See the Terms and Conditions (https://onlinelibrary.wiley.com/terms-and-conditions) on Wiley Online Library for rules of use; OA articles are governed by the applicable Creative Commons License

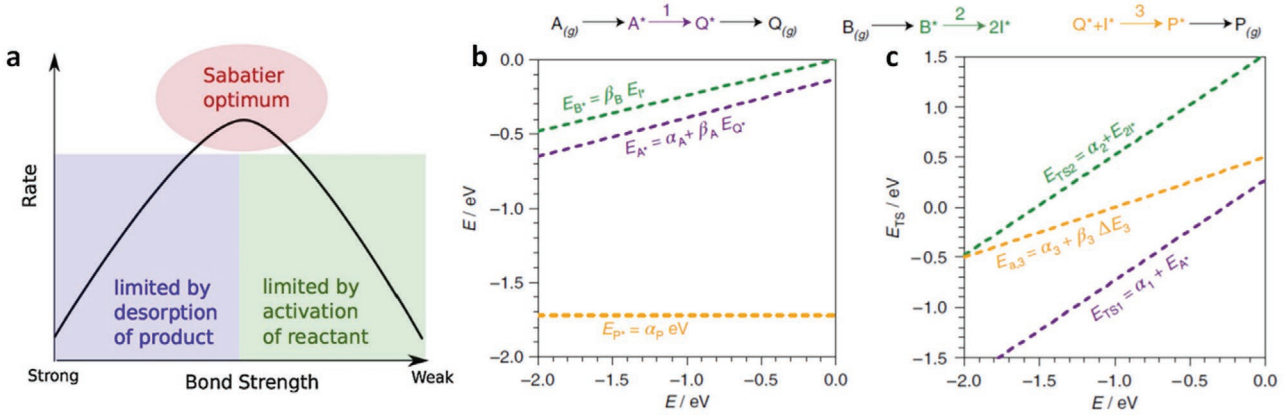

Figure 5. a) Illustration of the Sabatier principle. Reproduced with permission.[86] Copyright 2015, Elsevier Inc. b) Thermodynamic linear scaling relation. c) Kinetic linear scaling relation. Reproduced with permission.[87] Copyright 2019, Springer Nature.

2.2.2. Sabatier principle of Reaction Intermediates

For heterogeneous catalysis, the Sabatier principle indicates that too weak or too strong a binding energy to the reaction intermediates both result in a sluggish reaction rate, as shown in **Figure 5**a,[86] which results in a volcano-type relationship between the bond strength and the reaction rate.

For a complex reaction with multiple intermediates, the energies of intermediates are linked one to another in a linear relation, as shown in Figure 5b. Brønsted–Evans–Polanyi found that the kinetic terms depend linearly on the thermodynamic parameters, and thus, the activation barriers can be traced back to the energy of one or more intermediates in a linear form (Figure 5c). Electrochemical synthesis of NH_3 is severely limited by the linear scaling between the energetics of two key adsorbates, $*N_2H$ and $*NH_2$. To avoid or break or circumvent the scaling relation, some strategies were developed for reducing the fundamental overpotential. Yan et al. used bismuth (Bi) nanocrystals rather than a transition metal to avoid the scaling relationship. The Bi in combination with potassium cations achieved a high Faradaic efficiency of 66% due to the ideal electronic structure of Bi and its high selectivity.[88] Chen et al. reported that they introduced LiH as a second catalytic site into the transition metal-mediated catalyst, where the activated N atoms can be removed from the surface of the transition metal (TM) by the negatively charged H atoms of LiH, thereby achieving unprecedented catalytic activity.[89]

2.2.3. Activity Volcano Plots

Based on the Sabatier principle and scaling relation, the free energy diagrams and volcano plots can be constructed to screen the new catalysts for ammonia synthesis. In **Figure 6**a, the N* binding energy is described as the descriptor of both the HER and the NRR, and the limiting potential for the NRR and HER as a function of the N* binding energy.[90]

Computational screening of metal oxides was first conducted to predict potential active electrocatalysts.[74,91] For instance, the electrochemical NRR was theoretically studied on a range of transition metal oxides, including IrO_2, NbO_2, OsO_2, ReO_2, RuO_2, TaO_2, PtO_2, RhO_2, CrO_2, TiO_2, and MnO_2 under ambient conditions. Firstly, for different rutile oxides, the free energy landscape was calculated on the reduced, the H-term, and the O-term surface respectively. The step with the high change in free energy was identified as the potential-determining step (PDS). Then, taking into account two PDSs (including $N_2 \rightarrow *N_2H$ and $*NH_2 \rightarrow NH_3$), a volcano plot was constructed. Except

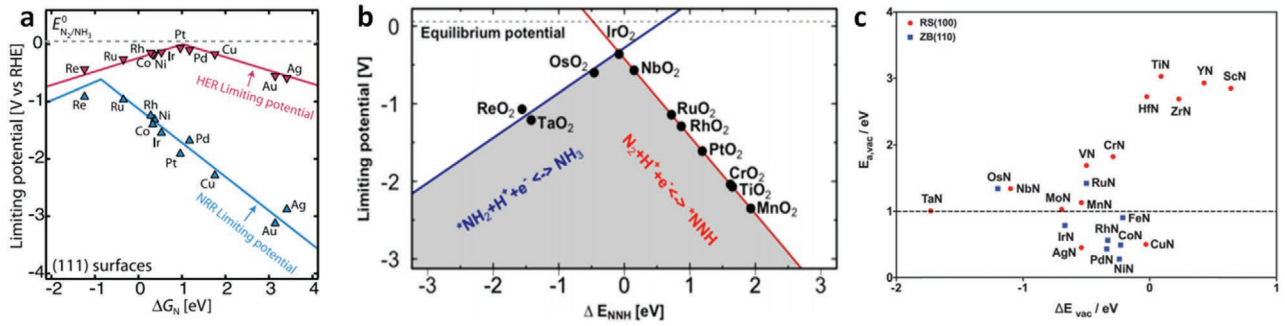

Figure 6. a) Comparison of NRR and HER limiting-potential volcanoes. Reproduced with permission.[90] Copyright 2015, Wiley-VCH. b) Potential determining step for electrochemical NH_3 formation on each metal oxide is plotted against the binding energy of NNH.[91] c) Energy difference (ΔE_{vac}) of a vacancy in the surface layer and in the first subsurface layer of a nitride, and the associated activation barrier of vacancy migration ($E_{a,vac}$). Reproduced with permission.[92] Copyright 2017, Elsevier Inc.

 © 2021 Wiley-VCH GmbH

23669608, 2021, 11, Downloaded from https://onlinelibrary.wiley.com/doi/10.1002/smtd.202100460 by University Town Of Shenzhen, Wiley Online Library on [26/11/2025]. See the Terms and Conditions (https://onlinelibrary.wiley.com/terms-and-conditions) on Wiley Online Library for rules of use; OA articles are governed by the applicable Creative Commons License

for ReO_2 and TaO_2, the dissociation of N_2 would be endergonic. $*NH_2 \rightarrow NH_3$ is the PDS for ReO_2 and TaO_2. In consideration of the competing HER reaction, the researchers finally concluded that ReO_2 and TaO_2 favor NNH adsorption over hydrogen adsorption, and thus can achieve higher yields of ammonia.

Similarly, a series of earlier transition metal mononitrides of Sc, Ti, V, Cr, Mn, Y, Zr, Nb, Mo, Hf, Ta, W, and Re were also investigated for NRR activity (Figure 6b and 6c). The free energy of all intermediates was first calculated, then the PDS was determined, and finally the onset potential necessary for nitrogen activation on each different metal nitride was accordingly estimated.[92] Apart from ScN, YN, and TaN, other (111) nitride surfaces showed more selectivity toward the NRR than the HER. In consideration of the onset potential and poisoning effect, only NbN was a promising candidate, which could endure the catalytic cycle of nitrogen activation and ammonia formation.

Other similar research on mononitrides of Zr, Nb, Cr, Mo, and V for the NRR also was reported.[50,51,74] The heterogeneous MvK mechanism was used to calculate the N_2 dissociation barrier, quantify the PDS, determine the thermodynamic barriers for N vacancy diffusion into the bulk, investigate the poisoning effect, and estimate the required potential for removal of any oxygen atoms that may adsorb onto the surface. The computation results suggested that special single-crystal surfaces were necessary for ZrN, NbN, and CrN to avoid the decomposition of the polycrystalline surfaces. The decomposition of a polycrystalline catalyst of VN could be prevented, however, when a low bias of up to −0.5 V versus SHE was applied and formed NH_3 only on the RS (100) facets.

3. Rational Design Strategies for Electrocatalysts

The electrocatalysts as the most important component for efficient electrochemical NH_3 synthesis, have been explored continuously, including metal oxides,[93–96] metal nitrides,[97,98] metal sulfides,[99,100] carbon materials,[101,102] etc. In addition, thanks to the advanced structural and electronic advantage, the 2D material plays an important role in the field of catalysis due to the advanced structural and electronic advantage, such as MXene,[103] phosphorene,[104] bismuthine,[105] and antimonene.[106] It can not only be used as the catalyst directly, but also serve as the substrate for atomic catalyst.[107] Various strategies, such as heteroatom doping, vacancy engineering, alloys, and interface engineering were also developed to improve the intrinsic catalytic activity and selectivity toward NH_3 synthesis

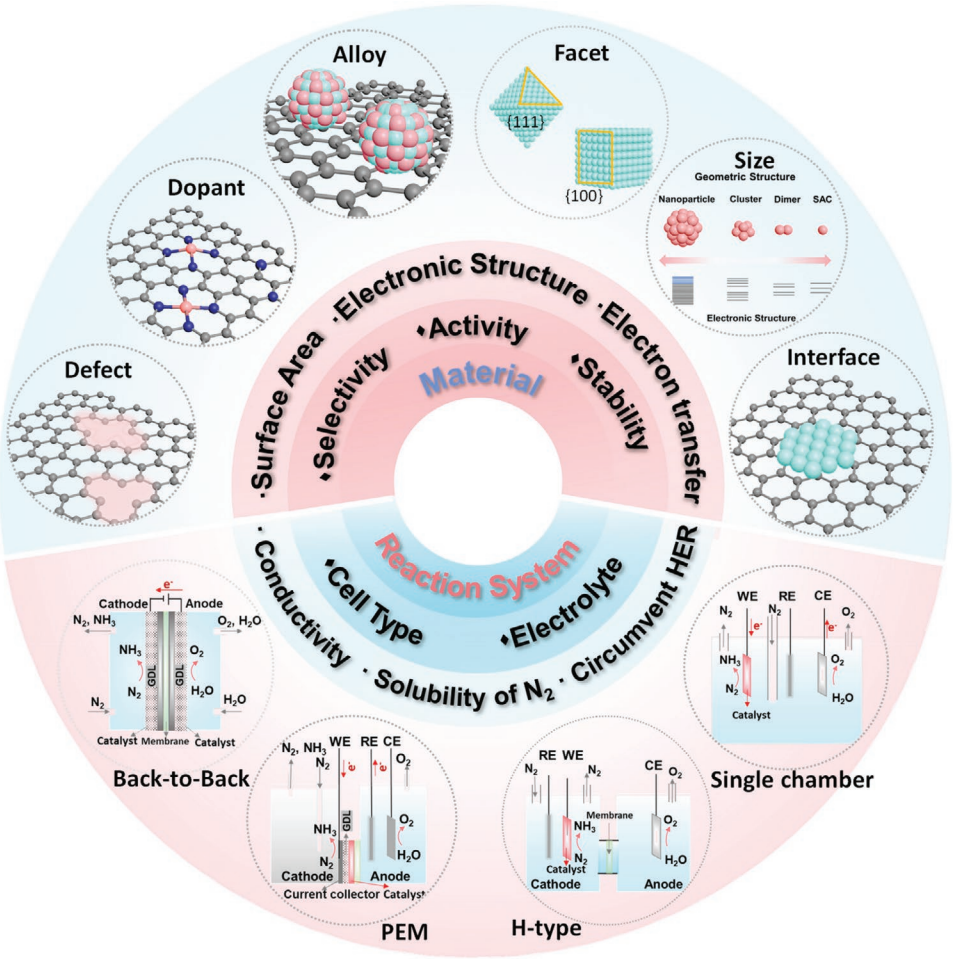

Figure 7. Typical strategies for engineering nanomaterials and device design for enhancing electrocatalytic performance.

 © 2021 Wiley-VCH GmbH

23669608, 2021, 11, Downloaded from https://onlinelibrary.wiley.com/doi/10.1002/smtd.202100460 by University Town Of Shenzhen, Wiley Online Library on [26/11/2025]. See the Terms and Conditions (https://onlinelibrary.wiley.com/terms-and-conditions) on Wiley Online Library for rules of use; OA articles are governed by the applicable Creative Commons License

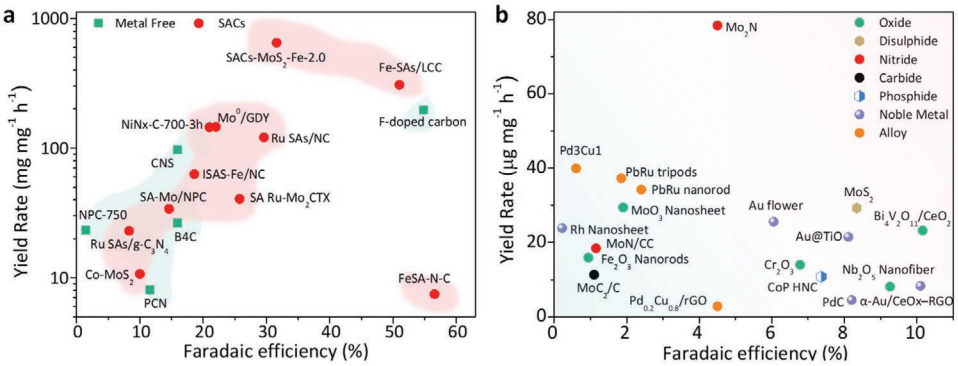

Figure 8. Comparison of the yield rate and Faradaic efficiency with recently reported NRR electrocatalysts. a) Metal-free or single-atom catalyst (SAC)-based electrocatalysts. b) Other nanomaterial electrocatalysts. Values were plotted from references (Tables 4 and 5).

via different reaction routes (**Figure 7**). In the sections below, we will elaborate these strategies for efficiently tuning the geometric structure and electronic structure, so as to further improve the NH_3 yield rate and Faradaic efficiency. And the partial catalysts' performance were summarized in **Figure 8**, **Table 4** and **Table 5**.

3.1. Defect Engineering

Both experimental and theoretical studies have demonstrated that the defect derived by the removal of heteroatom from surface of a material is active for different electrochemical reactions.[41–43] The presence of the defect will strongly influence its chemical properties and electronic structure, and could increase the exposure of active sites resulting from cracking of the surface.[153–155] The oxygen vacancies in BiOBr, TiO_2, and CuCr-layered double hydroxide (LDH) have been confirmed, which can provide coordinatively unsaturated sites for chemisorption of nitrogen molecules in the NRR photocatalysts.[156–158]

Lv et al., for the first time, introduced the nitrogen vacancies (NVs) into polymeric carbon nitride (PCN), which enabled a strong activation for N_2 as the NV can modulate the π-electron delocalization in the conjugated system of PCN.[108] Compared with the pristine PCN, the NV-PCN exhibited stronger adsorption of N_2, higher Faradaic efficiency, and a higher yield rate. The evidence based on calculations revealed that, in the electron transfer behavior, the electron on the adjacent carbon atom is transferred to the adsorbed N_2 and results in an increased bond length for N_2 (**Figure 9**a–d). The free energy diagram also confirmed that the NRR process on the VN-PCN also followed the alternating hydrogen mechanism (Figure 9e). The NRR performance of VN-PCN is even comparable to those of metal-based electrocatalysts, which achieved 8.09 mg h^{-1} mg^{-1} and Faradaic efficiency of 11.59% at –0.2 V versus reversible hydrogen electrode (RHE). Additionally, the joint effect of the dopant and defect usually act together to improve the electrocatalytic performance.

Liu et al. developed N-doped porous carbon (NPC) for NRR application, and the ammonia yield rate of NPC-750 (1.00–1.40 mmol g^{-1} h^{-1} or 0.60–0.84 μmol cm^{-2} h^{-1} at –0.7 to –0.9 V) was even higher than those of Ru-, Au-, and Fe/ carbon nanotube (CNT) electrocatalysts (0.012–0.097 μmol cm^{-2} h^{-1}). The as-prepared NPC exhibited high N_2 adsorption capability as its abundant pore structure was suited to fast mass transfer for adsorbing N_2 and N≡N cleavage.[102] DFT computations also confirmed that the pores can stabilize the N_2 reduction intermediate (NH_x and N_2H_x), which can produce high partial pressure and promote further reactions. The pyridinic and pyrrolic N also plays an important role in promoting ammonia synthesis. The preferable pathway was found to be $*N{\equiv}N \rightarrow *NH=NH \rightarrow *NH_2{-}NH_2 \rightarrow 2NH_3$.

3.2. Heteroatom Doping

Heteroatom doping has been widely used to tailor the physicochemical properties of catalyst materials. The unique electronic structures of heteroatom-doped materials will result in different adsorption energies, reaction thermodynamics, and activation barriers, and further influence the catalytic properties.[35,159–162] Typically, heteroatom doping engineering is divided into two categories: non-metal-atom doping (such as N-, B-, O-, S-, and P-doped materials)[33–35] and metal-atom doping (such as single atom Pd, Au, Mo, Fe, Pt and Co-doped materials).[44–49,163]

3.2.1. Metal-Atom Doping

Reasoning from theory and experimental results, downsizing the metal species to the sub-nanometer scale can achieve maximum atomic utilization efficiency in catalytic application.[164–167] Generally, nitrogen and metal are co-doped on carbon material, since the heteroatom doped defect-rich carbon can efficiently anchor metal atoms. In the case of single atom catalysts (SACs), the metals are low coordinated, so that they can strongly adsorb N_2 and effectively activate N_2. Recently, SACs also were developed for the NRR through theoretical and experimental study.[168] For instance, Zhao et al. systematically studied the potential of transition metal (TM) atoms (TM = Sc to Zn, Mo, Ru, Rh, Pd, and Ag) supported on defect-rich boron nitride (BN) as NRR catalysts via DFT calculations.[169] This work proposed three criteria for an eligible NRR electrocatalyst. By comparing the Gibbs free energy change (ΔG) of N_2 adsorption, the stabilization of N_2H*, and the destabilization of NH_2* species on different TM atoms, the researchers found that the Mo-embedded BN monolayer was the only eligible catalyst. The computation further revealed that the introduction of Mo atoms

© 2021 Wiley-VCH GmbH

23669608, 2021, 11, Downloaded from https://onlinelibrary.wiley.com/doi/10.1002/smtd.202100460 by University Town Of Shenzhen, Wiley Online Library on [26/11/2025]. See the Terms and Conditions (https://onlinelibrary.wiley.com/terms-and-conditions) on Wiley Online Library for rules of use; OA articles are governed by the applicable Creative Commons License

Table 4. Summary of metal-free catalysts.

Category	Materials	Electrolyte	Yield rate [V vs RHE]	FE [%] [V vs RHE]	Refs.
Metal-free catalyst	PCN	0.1 M HCl	8.09 [μg h^{-1} mg^{-1}]@–0.2 V	11.59@–0.2 V	[108]
	NCM	0.1 M HCl	0.08 [g m^{-2} h^{-1}]@–0.3 V	5.2@–0.2 V	[109]
	BC_3	0.05 M H_2SO_4	9.8 [mg h^{-1} cm^{-2}]@ –0.5 V	10.8@–0.5 V	[110]
	B_4C	0.1 M HCl	6.57 [μg h^{-1} mg^{-1}]@ –0.75 V	15.95@–0.75 V	[111]
	F-doped carbon	0.05 M H_2SO_4	197.7 [μg h^{-1} mg^{-1}]@–0.3 V	54.8@–0.2 V	[112]
	FC	0.05 M H_2SO_4	6.9 [μg h^{-1} cm^{-2}]@ –0.55 V	12.1@–0.55 V	[113]
	BP	0.01 M HCl	31.27 [μg h^{-1} mg^{-1}]@–0.7 V	5.07@–0.6 V	[114]
	BNS	0.1 M Na_2SO_4	13.22 [μg h^{-1} mg^{-1}]@–0.80 V	4.04@–0.8 V	[115]
	Eex-COF/NC	0.1 M KOH	12.53 [μg h^{-1} mg^{-1}]@–0.2 V	45.43@–0.2 V	[116]
	NPC	0.05 M H_2SO_4	1.4 [mmol g^{-1} h^{-1}]@ –0.9 V	1.42@–0.9 V	[102]
2D Material	$Ti_3C_2T_x$	1 M HCl 0.5 M Li_2SO_4	0.53 [μg h^{-1} cm^{-1}]@–0.5 V	5.78@–0.2 V	[103]
	N-phosphorene	0.1 M KOH	18.79 [μg h^{-1} mg^{-1}]@ 0 V	21.51@ 0 V	[104]
	Bi NS	0.1 M Na_2SO_4	13.23 [μg h^{-1} mg^{-1}]@ –0.8 V	10.46@–0.8 V	[105]
	Antimonene	0.1 M KOH	180.4 [g h^{-1} mg^{-1}]@–0.1 V	11.6%@ 0.05 V	[106]
	FeMo@NG	0.25 M $LiClO_4$	14.95 [μg h^{-1} mg^{-1}]@–0.4 V	41.7@–0.2 V	[117]
SACs	Ru-ST-12	KOH/KNO_3	5.56 [mol g^{-1} h^{-1}]@–0.8 V	100@–0.1 V	[78]
	SA-Mo/NPC	0.1 M KOH	34.0 [μg h^{-1} mg^{-1}]@–0.3 V	14.6@–0.3 V	[118]
	Mo^0/GDY	0.1 M Na_2SO_4	145.4 [μg h^{-1} mg^{-1}]@–1.2 V vs SCE	21@–1.2 V vs SCE	[119]
	Fe-SAs/LCC/GC	0.1 M KOH	307.7 [μg h^{-1} mg^{-1}]@–0.15 V	51.0@–0.15 V	[120]
	FePC	0.1 M Na_2SO_4	137.95 [μg h^{-1} mg^{-1}]@–0.3 V	10.50@–0.3 V	[121]
	ISAS-Fe/NC	0.1 M PBS	62.9 [μg h^{-1} mg^{-1}]@–0.4 V	18.6@–0.4 V	[122]
	SACs-MoS_2-Fe-2.0	0.1 M KCl	36.1 [mmol h^{-1} g^{-1}]@–0.2 V	31.6@–0.2 V	[123]
	FeSA-N-C	0.1 M KOH	7.48 [μg h^{-1} mg^{-1}]@ 0 V	56.55@ 0 V	[124]
	Ru SAs/g-C_3N_4	0.5 M NaOH	23.0 [g h^{-1} mg^{-1}]@ 0.05 V	8.3@ 0.05 V	[125]
	Ru/NC	0.1 M HCl	3.67 [mg h^{-1} mg^{-1}]@–0.21 V	7.5@–0.21 V	[126]
	Ru SAs/N-C	0.05 M H_2SO_4	120.9 [μg h^{-1} mg_{Ru}^{-1}]@–0.2 V	29.6@–0.2 V	[127]
	Au SAs-NDPs	0.1 M HCl	2.32 [μg h^{-1} cm^{-1}]@–0.2 V	12.3@–0.2 V	[128]
	Au_1/C_3N_4	5×10^{-3} M Na_2SO_4	1305 [μg h^{-1} mg_{Au}^{-1}]@–0.1 V	11.1@–0.1 V	[129]
	Ni-N_x-C-700	0.1 M KOH	115.0 [μg cm^{-2} h^{-1}]@–0.8 V	21.0@–0.8 V	[130]
	Co–MoS_2	0.01 M H_2SO_4	5.76 [μg h^{-1} mg^{-1}]@–0.3 V	1.7@–0.3 V	[131]

resulted in a large and localized spin moment and a decreased band gap for the Mo-embedded BN, which was reflected in activation of the N_2 molecule and a lower overpotential of the NRR process. The computational overpotential (η) of the distal, alternating, and enzymatic pathways were found to be 0.59, 0.72, and 0.19 V respectively, suggesting that the NRR process prefers to follow the enzymatic mechanism.[169]

Tao and co-workers reported that single-atom Ru anchored on N-doped graphene could achieve a high NH_3 yield rate of 3.665 mg_{NH3} h^{-1} $mg^{-1}{}_{Ru}$.[126] The addition of ZrO_2 in Ru@NC can also significantly improve the NRR Faradaic efficiency due to its suppression effect toward the HER. The optimized calculation models for Ru@$Zr_{32}O_{63}$ and Ru/NC are shown in **Figure 10**a. DFT calculations revealed the mechanisms of the HER and the NRR over Ru@$Zr_{32}O_{63}$ and Ru/NC_2, respectively (Figure 10b,c). Obviously, the Ru@$Zr_{32}O_{63}$ has a smaller ΔG (*H) of –0.20 eV than even Ru@NC (–0.42 eV), which indicates that H adsorption is significantly suppressed by the Ru@$Zr_{32}O_{63}$ with O vacancy.[126] Recently, Qiao's group built up a picture of 60 kinds of single transition metal atoms (TM-SACs) supported on N-doped carbon as NRR catalysts via DFT calculations. And the calculated model and reaction pathways are illustrated in Figure 10d,f, and all the involved transition metals are listed in Figure 10e. Based on the N adatom adsorption energy, the intrinsic activities of a series of TM-SACs were plotted in Figure 10g. And this work provides a promising strategy for designing effective TM-SACs-based catalysts to guide future NRR study. Yang et al used the monolayer MoS_2 as the substrate to anchor TM-SACs (TM = Ag, Au, Co, Cr, Cu, Fe, Mn, Mo, Ni, Pd, Pt, Rh, Ru, Sc, Ti, V, W, and Zn) toward NRR. Through the first-principles high-throughput screening, the study suggests the Mo atom anchored on the top of Mo site of MoS_2 possesses the most promising catalyst with a calculated overpotential of 0.28 V.[171]

 © 2021 Wiley-VCH GmbH

23669608, 2021, 11, Downloaded from https://onlinelibrary.wiley.com/doi/10.1002/smtd.202100460 by University Town Of Shenzhen, Wiley Online Library on [26/11/2025]. See the Terms and Conditions (https://onlinelibrary.wiley.com/terms-and-conditions) on Wiley Online Library for rules of use; OA articles are governed by the applicable Creative Commons License

Table 5. Summary of representative electrocatalysts for the NRR.

Category	Catalyst	Electrolyte	Yield rate [V vs RHE]	FE [%] [V vs RHE]	Refs.
Metal oxides	MoO_3 Nanosheet	0.1 M HCl	29.43 [μg h^{-1} mg^{-1}]@–0.5 V	1.9@–0.3 V	[29]
	Nb_2O_5 Nanofiber	0.1 M HCl	8.09 (μg h^{-1} mg^{-1}) @–0.55 V	9.26@–0.55 V	[94]
	Fe_2O_3 Nanorods	0.1M Na_2SO_4	15.9 [μg h^{-1} mg^{-1}]@–0.8 V	0.94@–0.8 V	[132]
	Nano Fe_2O_3	0.5 NaOH/ 0.5 KOH NaOH/0.5 KOH NaOH/0.5 KOHNaOH/0.5 KOH	N/A	35@ 2 mA cm^{-2}	[28]
	Fe_2O_3@CNT	$KHCO_3$	2.2×10^{-3} [g m^{-2} h^{-1}] @ -2.0 V vs Ag/AgCl	≈0.15 @ -1.0 V vs Ag/AgCl	[25]
	30%wt Fe_2O_3@CNT	0.5 M KOH	1.06×10^{-11} [mol cm^{-2} s^{-1}] @–2.0 V vs Ag/AgCl	0.16 @–2.0 V vs Ag/AgCl	[133]
	o-Fe_2O_3–Ar/CNT	0.1 M KOH	0.46 [mg h^{-1} cm^{-2}]@–0.9 V vs Ag/AgCl	6.04 @–0.9 V vs Ag/AgCl	[134]
	$Bi_4V_2O_{11}/CeO_2$	HCl	23.21 [μg h^{-1} mg^{-1}]@–0.2 V	10.16@–0.2 V	[95]
	TiO_2 nanosheet	0.1 M Na_2SO_4	9.16×10^{-11} mol s^{-1} cm^{-2} @-0.7 V	2.50@–0.7 V	[135]
Metal sulfides	MoS	1.0 M KOH	75.85 [μg h^{-1} cm^{-1}]@ –1.0 V	0.098@–1.0 V	[100]
	FeS	1.0 M KOH	185.1[μg h^{-1} cm^{-1}]@–1.0 V	0.105@–1.0 V	[100]
	NiS	1.0 M KOH	237.1 [μg h^{-1} cm^{-1}]@–1.0 V	0.849@–1.0 V	[100]
	ZnS	1.0 M KOH	345.96 [μg h^{-1} cm^{-1}]@–1.0 V	0.964@–1.0 V	[100]
	CdS	1.0 M KOH	253.37 [μg h^{-1} cm^{-1}]@–1.0 V	0.741@–1.0 V	[100]
	MoS	0.1 M Li_2SO_4	43.4 [μg h^{-1} cm^{-1}]@–0.2 V	9.81@ –0.2 V	[99]
Metal nitrides	MoN nanosheet	0.1 M HCl	3.01×10^{-10} mol s^{-1} cm^{-2}@–0.3 V	1.15@–0.3 V	[97]
	VN nanowire	0.1 M HCl	2.48×10^{-10} mol^{-1} s^{-1} cm^{-2}@–0.3 V	3.59@–0.3 V	[136]
Metal phosphide	CoP HNC	1.0 M KOH	10.78 [μg h^{-1} mg^{-1}]@–0.4 V	7.36@ 0 V	[137]
Noble metals	Au THH NR	0.1 M KOH	1.65 [μg h^{-1} cm^{-2}]@ –0.2 V	3.879@–0.2 V	[26]
	Au Sub-nanoclusters@TiO	0.1 M HCl	21.4 9 [μg h^{-1} mg^{-1}]@–0.2 V	8.11@–0.2 V	[138]
	α-Au/CeO_x–RGO	0.1 M HCl	8.3 [μg h^{-1} mg^{-1}]@–0.2 V	10.10@–0.2 V	[139]
	Au nanocage	0.5 M $LiClO_4$	3.9 [μg h^{-1} cm^{-2}]@–0.5 V	30.2@–0.5 V	[140]
	Ru nanoparticles	0.01M HCl	≈5.5 mg h^{-1} m^{-2}@–0.1 V	5.4@–0.01 V	[29]
	Ru/C	2 M KOH	0.25 [μg h^{-1} cm^{-2}]@–0.96 V	0.92@–0.96 V	[24]
	Rh nanosheet	0.1 M KOH	23.88 [μg h^{-1} mg^{-1}]@–0.2 V	0.217@–0.2 V	[141]
	Pt/C	0.1 M Li_2SO_4	9.37×10^{-10} mol s^{-1} cm^{-2}@–1.2 vs Ag/AgCl	0.83	[142]
	Ir	6M KOH/polyacrylic acid homopolymer	2.14×10^{-11} (mol cm^{-2} s^{-1})@ cell voltage of 0.25 V	0.01 @ Cell voltage of 0.25 V	[143]
	Ru/Ti	0.5 M H_2SO_4	7.31 (μg h^{-1} cm^{-2})@ 2 mA cm–^{2}	N/A	[144]
	Rh/Ti	0.5 M H_2SO_4	0.918 [μg h^{-1} cm^{-2}]@ 2 mA cm^{-2}	N/A	[144]
	Pd	SrCe0.9 Yb0.05O3	0.18 mol h^{-1} m^{-2}	N/A	[145]
	Ni wire	0.1 M LiCl/EDA	7.73×10^{-7} mol h^{-1} cell voltage of 1.8 V	17.2 cell voltage of 1.8 V	[146]
	Cu	0.2 M $LiClO_4$/0.18 M ethanol in THF	N/A	5.3	[147]
	Pt/C	Admixed NH^{4+} /H^+ conducting Nafion 211 (Solid State Electrolyte)	1.14×10^{-9} mol s^{-1} cm^{-2} Cell voltage of 1.6 V	0.55 Cell voltage of 1.6 V	[148]
Alloys	Pd_3Cu_1	1 M KOH	39.9@–0.25 V	1.22%@–0.25 V	[149]
	$Pd_{0.2}Cu_{0.8}$/rGO	0.1 M KOH	2.8 [μg h^{-1} mg^{-1}]@–0.2 V	≈4.5 @ 0.0	[150]
	RuPt	1.0 M KOH	1.08 [g s^{-1} cm^{-2}]@ 0.023 V	13.2 @ 0.123 V	[151]
	PbRu nanorod	0.1 M HCl	34.2 [μg h^{-1} mg^{-1}]@–0.2 V	2.4@–0.2 V	[152]

© 2021 Wiley-VCH GmbH

23669608, 2021, 11, Downloaded from https://onlinelibrary.wiley.com/doi/10.1002/smtd.202100460 by University Town Of Shenzhen, Wiley Online Library on [26/11/2025]. See the Terms and Conditions (https://onlinelibrary.wiley.com/terms-and-conditions) on Wiley Online Library for rules of use; OA articles are governed by the applicable Creative Commons License

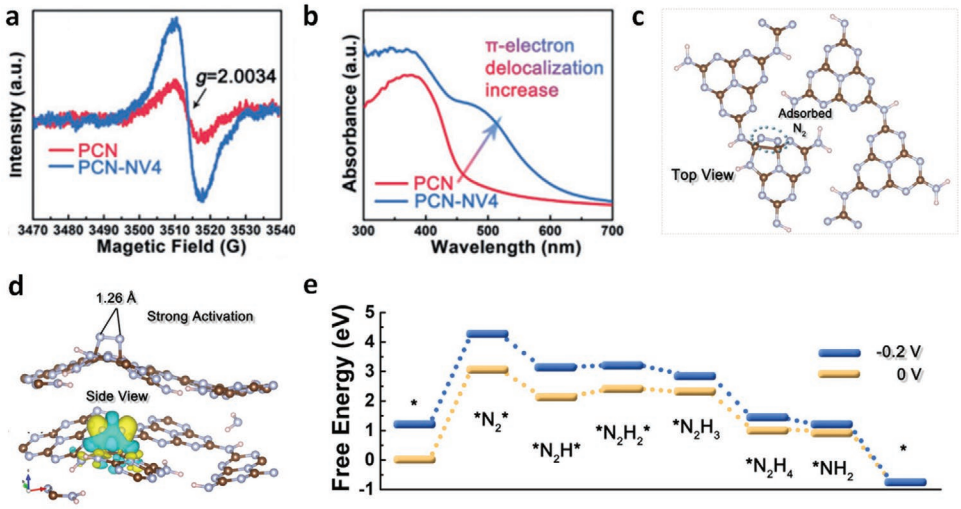

Figure 9. Defect engineering. a) EPR spectra. b) UV–vis DRS. c) N_2 adsorption geometry on polymeric carbon nitride (PCN) with nitrogen vacancy (NV). d) The charge density difference of the N_2-adsorbed PCN with NVs. e) Free energy profile for the NRR on NV engineered PCN. Reproduced with permission.[108] Copyright 2018, Wiley-VCH.

3.2.2. Non-Metal-Atom Doping

Recently, different kinds of electrocatalysts including Fe, Mo, Pd, Cu, and Ru, have been verified to be the active centers for the NRR under the ambient conditions, although the high intrinsic activity toward the HER of these catalysts leads to low Faradaic efficiency and NH_3 yield. Thus, the metal-free catalysts emerged with unfavorable activity toward the HER.

To date, electron-deficient B and electronegative F are the usual atoms that are used to design metal free catalysts for the NRR.[112,172–178] The pioneering work demonstrated that, compared to a certain transition-metal, which can weaken the N≡N bond through π-donation, in several borylene complexes, the strong π-donation of B dopant to CO is also a bonding motif important to end-on dinitrogen binding to a metal center. The B-to-N π-back bonding formation provides a new pathway for

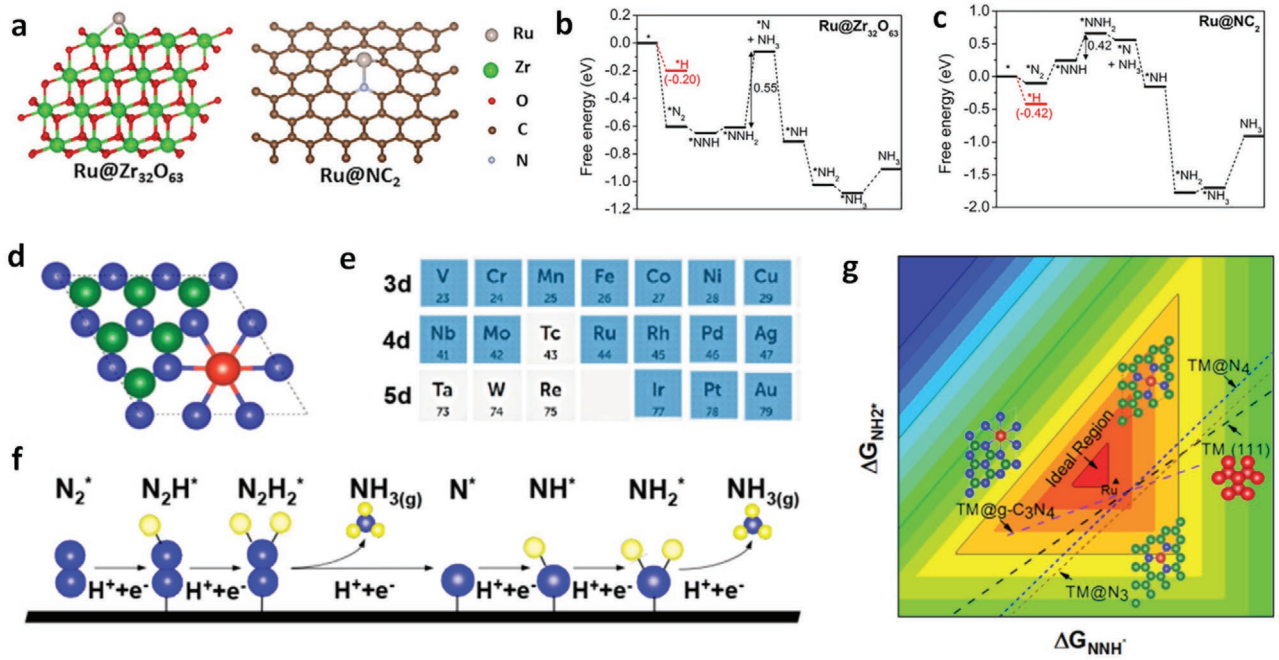

Figure 10. Heteroatom metal-atom doping. a) Calculation atomic structure models for Ru@$Zr_{32}O_{63}$ and Ru/NC. Free-energy diagram for the NRR on b) Ru@$Zr_{32}O_{63}$, and c) on Ru@NC. Reproduced with permission.[126] Copyright 2019, Elsevier Inc. d) Calculation models of single transition metal atom catalyst anchored on a g-C_3N_4 matrix. e) Metal elements (blue shades) for the eNRR activities obtained experimentally. f) Schematic illustration of proton-coupled electron transfer for NRR via a distal pathway. g) Comprehensive comparisons of the limiting potential of SACs consisting of different metal centers and supports, with the pure metal (111) surface included as a reference. Reproduced with permission.[170] Copyright 2019, American Chemical Society.

 © 2021 Wiley-VCH GmbH

23669608, 2021, 11, Downloaded from https://onlinelibrary.wiley.com/doi/10.1002/smtd.202100460 by University Town Of Shenzhen, Wiley Online Library on [26/11/2025]. See the Terms and Conditions (https://onlinelibrary.wiley.com/terms-and-conditions) on Wiley Online Library for rules of use; OA articles are governed by the applicable Creative Commons License

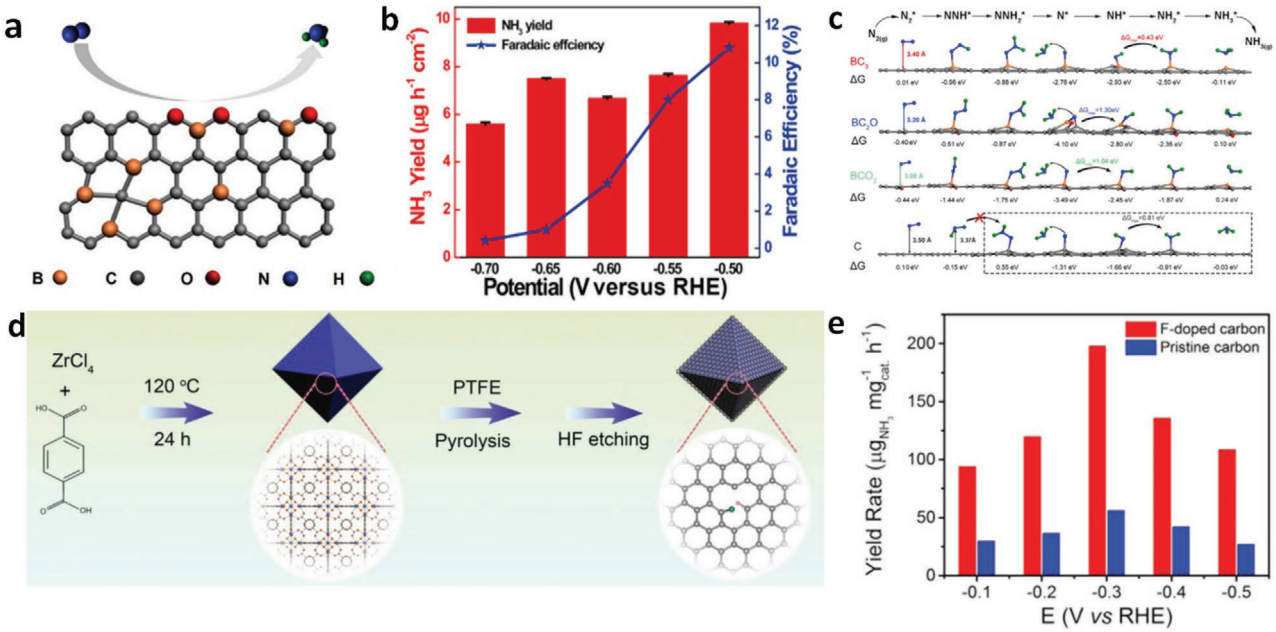

Figure 11. Heteroatom non-metal-atom doping. Electrocatalytic NRR activity of the boron doped graphene (BG): a) Schematic illustration of the NRR for BG. b) NH_3 production rates and FE_{NH3} of BG-1. c) Reaction pathways of the NRR on BC_3, BC_2O, BCO_2, and C. Reproduced with permission.[110] Copyright 2018, Elsevier Inc. d) Schematic illustration of the synthetic procedure for F-doped carbon. e) Yield rate of NH_3 over F-doped carbon and pristine carbon at different potentials. Reproduced with permission.[112] Copyright 2020, Wiley-VCH.

the NRR. In addition, under acidic conditions, the B atoms can prevent the binding of Lewis acid and H^+, which will suppress the competing HER reaction.[173] Qiu et al. also reported that boron carbide(B_4C) nanosheet acts as a high performance NRR catalyst, which can achieve a NH_3 yield of 26.57 g h^{-1} mg^{-1}_{cat} with a FE of 15.95% at –0.75 V versus RHE. The DFT computed energy profiles revealed that $*NH_2$–$*NH_2$→$*NH_2$–$*NH_3$ is the rate-limiting step.[111] Based on early studies of single-boron NRR catalysts,[102] B-atoms have been successfully introduced into the graphene to fix nitrogen (**Figure 11**a).[110] The theoretical and experimental studies mutually corroborate the N_2 catalytic ability of B-doped graphene (BC_3). This is because the smaller electronegativity of boron (2.04) is introduced into carbon (2.55), which results in a redistribution of electron density of both the highest occupied molecular orbital and the lowest unoccupied molecular orbital (LUMO). The positively charged B atoms serve as effective catalytic centers to form B–N bonds and further produce the NH_3. Furthermore, under acidic conditions, the bonding of Lewis acid with H^+ is prohibited on these electron-deficient boron sites. Therefore, compared with the undoped graphene, the NRR yield rate (9.8 mg h^{-1} cm^{-2}) and Faradaic efficiency (10.8%) of BG (Figure 11b) have fivefold and tenfold increases, respectively, due to the N_2 activation and the suppression of the competing side reaction (HER). First-principles calculations were carried out to understand the reaction mechanism. Among the different NRR pathways, the distal pathway in the associative mechanism stood out. The calculation results confirmed that the formation of the adsorbed intermediate NH_2* is the limiting step for BC_3 (0.43 eV, $NH*/NH_2$). Compared with the introduction of oxygen on B, BCO_2 (1.04 eV, N*/NH*), and BC_2O (1.30 eV, N*/NH*), the BC_3 possessed the lowest reaction energy barrier (0.43 eV), indicating that it had the best catalytic NRR performance among these structures (Figure 11c).

F element was also introduced into the 3D carbon framework for a highly efficient metal-free catalyst (Figure 11d).[112] The bonding between F and C atoms created a Lewis acid site which repelled the H proton, suppressing the activity of the HER. Moreover, the low activity toward the HER of the catalyst resulted in high Faradaic efficiency (FE) and a high yield rate for NH_3. During the N_2 electroreduction process, the F-doped carbon achieved the highest FE of 54.8% for NH_3 product at –0.2 V versus reversible hydrogen electrode (versus RHE), while the pristine carbon frameworks only reached 18.3%. Notably, at –0.3 V versus RHE, the yield rate of F-doped carbon for NH_3 reached 197.7 μg mg^{-1}_{cat} h^{-1} (Figure 11e). Such a value is more than one order of magnitude higher than those of other metal-free electrocatalysts under near-ambient conditions to date.

3.3. Size Effect

Since the NRR involves multiple reaction intermediates, it is rather challenging for a single-atom center to simultaneously improve the yield rate and the FE. To address this issue, a promising strategy is to introduce dimer sites to tune the adsorption of intermediates. Compared with single atoms, metal dimers and clusters are also cost-effective, with more active site exposure and high utilization efficiency.[180] Theoretically, Co, Ni, and Cu-based bi-atom catalysts (BACs) have been predicted to have much higher activity toward O_2 reduction, as compared with their single-atom counterparts.[181] Several metal dimers, including

© 2021 Wiley-VCH GmbH

23669608, 2021, 11, Downloaded from https://onlinelibrary.wiley.com/doi/10.1002/smtd.202100460 by University Town Of Shenzhen, Wiley Online Library on [26/11/2025]. See the Terms and Conditions (https://onlinelibrary.wiley.com/terms-and-conditions) on Wiley Online Library for rules of use; OA articles are governed by the applicable Creative Commons License

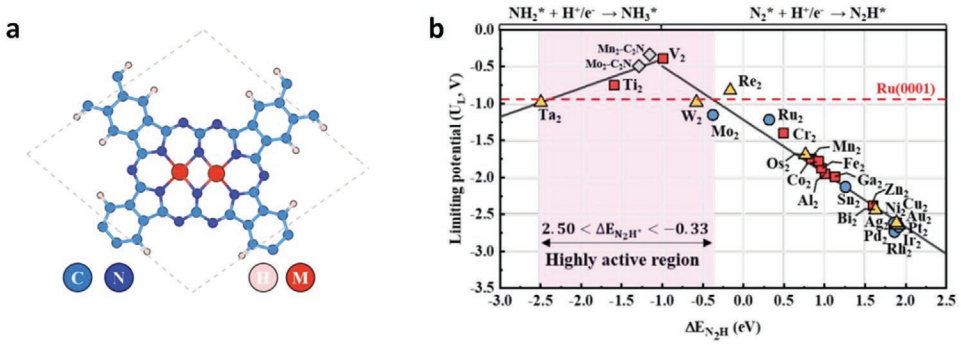

Figure 12. Size effect a) Structural model of 2D metal dimers supported on 2D expanded phthalocyanine (M_2-Pc) nanosheet. b) Volcano-shaped relationship between the theoretical limiting potential (U_L) and the adsorption energy of NNH*(ΔE_{N2H*}). Reproduced with permission.[179] Copyright 2020, American Chemical Society.

Mo_2 and Mn_2, supported by 2D C_2N monolayers, were predicted to have better catalytic activity than the corresponding SACs. Each metal atom combined with two pyrrole nitrogen atoms and two amino nitrogen atoms of the macrocycle to form the M_2N_6 moiety.[179] The authors used the C_2N as the substrate, and single atoms and double atoms of different metals (including Cr, Mn, Fe, Co, and Ni) were integrated into the C_2N, which were denoted as TM–C_2N, and TM_2–C_2N (**Figure 12**a). According to the thermodynamic, kinetic, and thermal stability studies, an active catalyst should have an appropriate adsorption energy of NNH* near –1.0 eV, and the Mn_2–C_2N was regarded as the most effective NRR catalyst. The NRR mechanisms over the Mn–C_2N and the Mn_2–C_2N were compared in the free energy profile. In the case of the Mn–C_2N, the reaction followed the distal pathway with the rate-determining step (RDS) the first H—N bond formation with a ΔG value of 0.69 eV. Mn_2–C_2N followed the enzymatic pathway with the same RDS of first H—N bond formation with a ΔG value of 0.08 eV. The NRR performance of Mn_2–C_2N is prompted by the bridge site of Mn_2–C_2N, which can make the adsorbed N_2 more active (Figure 12b). Note that the V_2–Pc, which displays the highest activity among all the considered homonuclear M_2–Pc.

3.4. Crystal-Facet Design

Crystal-facet engineering is also a promising strategy for improving the corresponding electrocatalytic activity.[51,182] A tremendous amount of research has demonstrated that the facet effect plays an important role in fine tuning the physicochemical properties of a catalyst (such as the energy level, Fermi level).[39,40] Atomic-level engineering will precisely manipulate the atomic arrangement and coordination of the active facets, and subsequently improve the corresponding catalytic activity.[183] Theoretical calculations have shown that the adsorption capability of intermediates varies with different facets in the NRR process.[67,90]

Wang et al. reported that Ru clusters with (002) facets can significantly enhance the NRR selectivity with a high yield rate of ≈5.5 mg h^{-1} m^{-2}.[29] A simplified hexagonal close packed (hcp) Ru (117) nanoparticle model was constructed to elucidate the reaction mechanism. The (001) surface, which is equivalent to (002), was composed of center atoms (yellow) and edge atoms (orange) (**Figure 13**a). The edge atoms exhibited stronger adsorption of N_2 than the center Ru atoms, indicating that the edge-sites can effectively activate the N≡N bonds. Furthermore, DFT calculations revealed that the reaction pathway prefers the dissociative mechanism (Figure 13b). $*NH_2 + H+/e^- \rightarrow *NH_3$ is the rate-limiting step with an uphill energy of 0.33 eV (Figure 13c).

Bao et al. used tetrahexahedral gold nanorods (THH Au NRs), enclosed by stepped 730 facets, which were composed of (210) and (310) subfacets as a heterogeneous NRR electrocatalyst (Figure 13d).[26] The abundant high-index facets (310) and (210) on the THH Au NRs provided a large number of active sites (Figure 13e), which could adsorb and dissociate N_2. It was concluded from the free energy diagram that the N_2 dissociation is the rate-determining, step while the other elementary reactions are exothermic, except for the formation of hydrazine hydrate from NH_2NH_2* intermediates (Figure 13f). The NRR process followed the alternating hydrogenation mechanism. Similarly, Nazemi et al. reported the synthesis of hollow gold nanocages (AuHNCs) by the galvanic replacement technique.[140] Impressively, the AuHNCs exhibited good NRR catalytic ability with FE of 30.2% at –0.4 V versus RHE and NH_3 yield of 3.9 μg cm^{-2} h^{-1} at –0.5 V versus RHE. The X-ray diffraction (XRD) and transmission electron microscope (TEM) results revealed the AuHNCs were composed of various surface index facets and sharper edges. A large amount of valency-unsatisfied surface atoms on the surface could serve as the active sites for the electrochemical NRR. Furthermore, when the operation temperature increased from 20 to 50 °C, the FE increased to 40.55% from 30.2% due to the faster mass transport rate.

3.5. Alloy

Alloying is another promising strategy, which can tune the surface strain and electronic interactions. Alloying engineering can precisely tune the binding strength of intermediates on a catalyst surface and further enhance the specific catalytic activity.[185] [37,38] A series of Ru-based alloys were extensively explored for ammonia synthesis, such as RuPt[151] and PdRu alloys,[152,186,187]which achieved a nice boost to performance over pure Ru.

Shi et al. developed PdCu amorphous nanoclusters anchored on reduced graphene oxide (rGO) as an NRR catalyst. The $Pd_{0.2}Cu_{0.8}$/rGO was synthesized by co-reducing the graphene oxide (GO), Pd, and Cu precursors using tannic acid and

© 2021 Wiley-VCH GmbH

23669608, 2021, 11, Downloaded from https://onlinelibrary.wiley.com/doi/10.1002/smtd.202100460 by University Town Of Shenzhen, Wiley Online Library on [26/11/2025]. See the Terms and Conditions (https://onlinelibrary.wiley.com/terms-and-conditions) on Wiley Online Library for rules of use; OA articles are governed by the applicable Creative Commons License

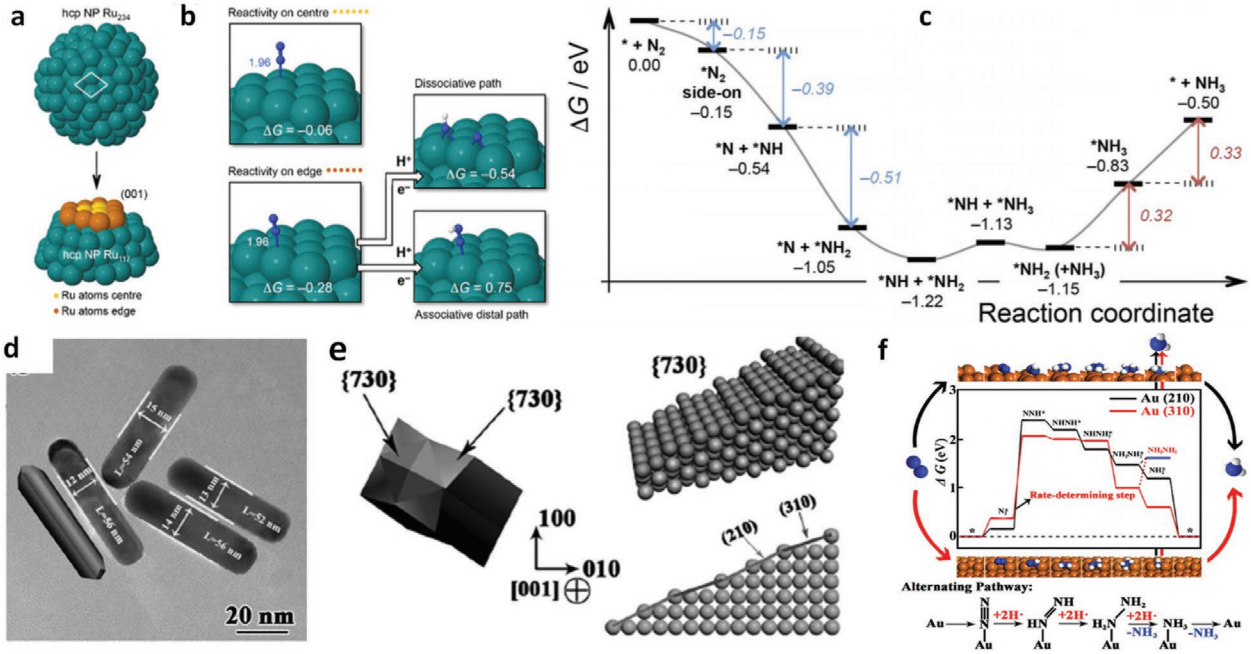

Figure 13. Crystal-facet design. a) The calculated models of hcp Ru_{234} and hcp Ru_{117} nanoparticles (NPs). b) Free energy change of different reaction pathways. c) Free energy profile of the NRR process over the Ru NPs. Reproduced with permission.[184] Copyright 2018, Wiley-VCH. d) TEM image of Au THH NRs. e) Atomic structure model of Au THH NRs with different exposed facets. f) Free energy profile of the NRR process over Au (210) and Au (310). Reproduced with permission.[26] Copyright 2016, Wiley-VCH.

$NaBH_4$. The XRD patterns without an obvious peak indicated the amorphous structure. The STEM images and X-ray photoelectron spectroscopy (XPS) spectra of $Pd_{0.2}Cu_{0.8}$/rGO confirmed the presence of CuPd alloy supported on rGO and the electron transfer between Pd and Cu. The synergistic electronic effect of the bimetal significantly improved the NRR catalytic activity. Since the electronic interaction between Pd and Cu led to changes in the electronic states of the monometals, the ammonia yield rate of $Pd_{0.2}Cu_{0.8}$/rGO was 2.1 fold and 2.4 fold higher than those of its Pd/rGO and Cu/rGO counterparts, respectively.[150]

To further optimize the performance of the alloy, the bimetallic mole ratio was tuned. Pang et al. prepared bimodal nanoporous Pd_3Cu_1 alloy with high active site density, good reactant accessibility, and structural integrity (**Figure 14**a).[149]

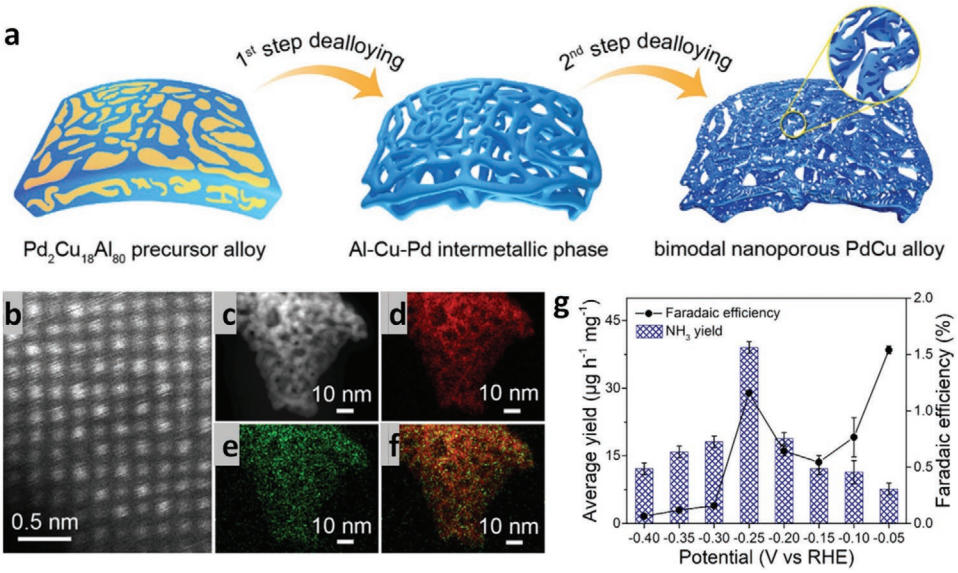

Figure 14. a) Illustration of the preparation of Pd_3Cu_1 alloy with hierarchically porous structure. b) HAADF–STEM image of Pd_3Cu_1 alloy. c–f) STEM–EDS mappings of Pd_3Cu_1 alloy. g) Yield rate and Faradaic efficiency of Pd_3Cu_1 alloy at different applied potentials. Reproduced with permission.[149] Copyright 2019, Elsevier Inc.

© 2021 Wiley-VCH GmbH

23669608, 2021, 11, Downloaded from https://onlinelibrary.wiley.com/doi/10.1002/smtd.202100460 by University Town Of Shenzhen, Wiley Online Library on [26/11/2025]. See the Terms and Conditions (https://onlinelibrary.wiley.com/terms-and-conditions) on Wiley Online Library for rules of use; OA articles are governed by the applicable Creative Commons License

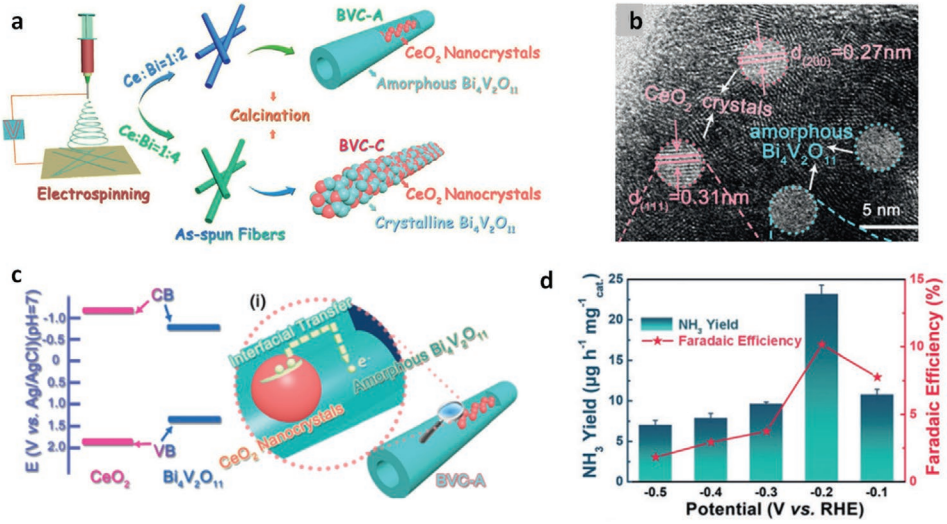

Figure 15. a) Scheme for the fabrication of $Bi_4V_2O_{11}/CeO_2$ hybrid with an amorphous phase (BVC-A) and the $Bi_4V_2O_{11}/CeO_2$ hybrid with crystalline phase (BVC-C) electrocatalysts. b) High-resolution TEM (HRTEM) image of BVC-A. c) Band alignment of $Bi_4V_2O_{11}$ and CeO_2. i) interfacial charge transfer in BVC-A. d) Yield of NH_3 and Faradaic efficiency at different potential. Reproduced with permission.[95] Copyright 2018, Wiley-VCH.

The Pd_3Cu_1 alloy displayed a bicontinuous nanoporous network of Pd and Cu elements uniformly distributed throughout the alloy (Figure 14b–f). The 3D interconnected hierarchical structure could dramatically promote the catalytic reaction between the reactant and the catalyst. Specifically, the presence of small pores could provide a large specific surface area with a high density of active sites to react with reactant molecules, while the large pores could facilitate timely and consistent transport of reactant molecules to active sites. This alloy exhibited a NH_3 production yield of 39.9 μg h^{-1} mg^{-1} at –0.2 V versus RHE and a Faradaic efficiency of 1.56% at –0.05 V versus RHE (Figure 14g).[149]

3.6. Phase Engineering

Phase engineering can tune the electronic state of a material and benefit its catalytic properties,[188,189] which has been verified and widely applied in the oxygen reduction reaction (ORR), the oxygen evolution reaction (OER),[190] and the HER.[191] Lv and co-workers reported that nitrogen fixation could be achieved using amorphous Au nanoparticles anchored on reduced graphene oxide (a-Au/CeO_x–rGO).[139] Compared to crystallized material, the amorphous structure is more active due to the presence of many "dangling bonds". Their experimental results confirmed that the a-Au/CeO_x–rGO exhibited excellent NRR catalytic performance thanks to the high content of unsaturated coordination sites.

Lv and co-workers also reported that the phase conversion of $Bi_4V_2O_{11}$ from crystalline to amorphous could be achieved by introducing CeO_2 (**Figure 15**a,b).[95] Energy-dispersive X ray (EDX) line scanning and mapping analysis revealed the homogeneous distribution of amorphous $Bi_4V_2O_{11}$. The availability of localized electrons in the amorphous phase could be enhanced for π-back donation, which contributes to the N_2 activation. Moreover, such configuration can accelerate the electrons transfer between CeO_2 and $Bi_4V_2O_{11}$ (Figure 15c). Benefiting from the reduced energy barrier in amorphous catalysts, remarkable NRR performance was achieved with a yield rate of 23.21 mg h^{-1} mg^{-1}_{cat} and Faradic efficiency of 10.16% at –0.2 V versus RHE (Figure 15d).

4. Reaction System and Electrolyte

Since the ammonia synthesis process involves multiple intermediates via different pathways, the HER is the major competing reaction, and N_2H_4 may be the by-product. These all make selectivity and efficiency the main challenge. Besides the rational design of the electrocatalyst mentioned above, to improve the selectivity and efficiency, the appropriate selection of the right equipment and electrolyte is also vital. Thus, from the selectivity and efficiency perspective, we summarize and classify the equipment types and electrolytes for better understanding of the influence of system design to enable the selection of more rational equipment and electrolyte (**Figure 16**).

4.1. Reaction Cell

The rational design of an electrochemical N_2 fixation system also plays an important role in improving the yield rate and faradic efficiency. Four kinds of cell configurations were developed for electrochemical N_2 fixation, including the back-to-back cell,[142,148,192] the polymer electrolyte membrane-type cell, which generally uses a solid-state electrolyte, the H-type cell, and the single chamber cell with liquid electrolyte.[193–197]

The back-to-back cell usually consists of two porous electrodes and one polymer membrane as the solid-state electrolyte. Generally, proton exchange membranes (PEMs) [148,192] and anion

© 2021 Wiley-VCH GmbH

23669608, 2021, 11, Downloaded from https://onlinelibrary.wiley.com/doi/10.1002/smtd.202100460 by University Town Of Shenzhen, Wiley Online Library on [26/11/2025]. See the Terms and Conditions (https://onlinelibrary.wiley.com/terms-and-conditions) on Wiley Online Library for rules of use; OA articles are governed by the applicable Creative Commons License

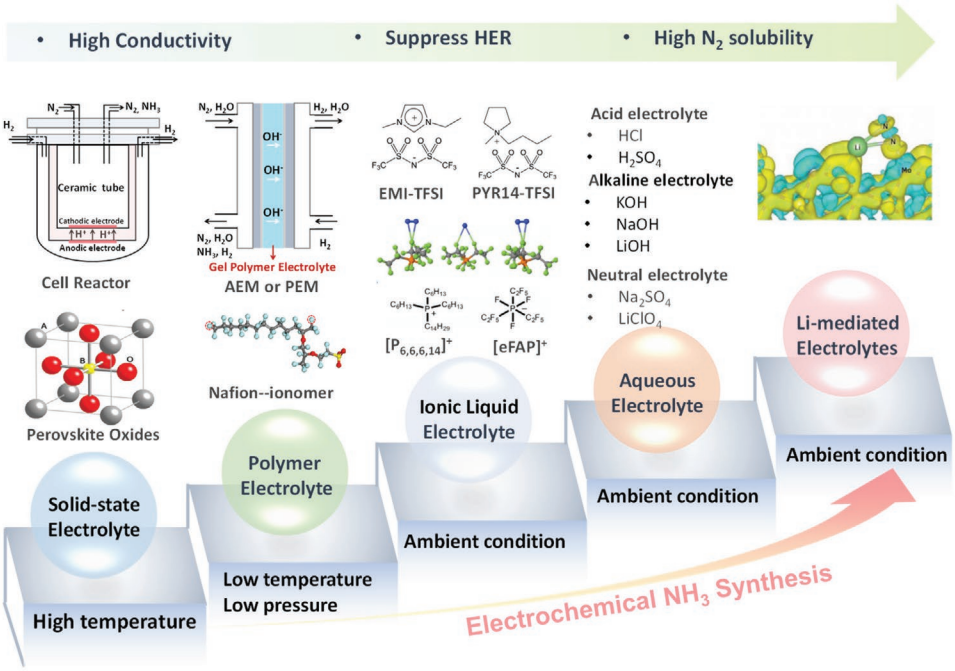

Figure 16. Overview of the electrolyte selection, from solid-state electrolyte to polymer electrolyte, ionic liquid electrolyte, and aqueous electrolyte, as well as Li-mediated electrolyte. Reproduced with permission.[145] Copyright 1998, The American Association for the Advancement of Science. Reproduced with permission.[99] Copyright 2019, Wiley-VCH.

exchange membranes (AEMs)[20,198] are used for acid and basic cell environments, respectively. Besides the solid-state electrolyte, liquid electrolyte also can be applied in the back-to-back type cell. Compared to the back-to-back cell, the addition of liquid electrolyte in the polymer electrolyte membrane-type (PEM-type) cell not only can ensure the full wetting of the membrane and increases its conductivity, but a reference electrode can also be used to detect the potential of the working electrode.[24,197]

The H-type cell is separated by a Nafion membrane into two chambers filled with liquid electrolyte, where the working and reference electrode can accurately detect the applied potential in the cathode. Bao and Nazemi both used the membrane electrode assembly (MEA) technology for the NRR process, which can limit the amount of water access to the catalyst surface and suppress the HER.[26,140] Recently, a single chamber was also developed for the NRR electrocatalytic system, which has a compact and simplified structure.[144,199–202] Both the H-type and the single-chamber cells both have the problem, however, that gaseous NH_3 or NH^{4+} may be oxidized at the anode.

4.2. Electrolyte Selection

The optimal electrolyte can increase the solubility of N_2, circumvent the HER, maintain the catalyst stability, and enhance the current efficiency. Generally, the electrolytes applied in NRR catalysis can be divided into four categories, including aqueous, nonaqueous, polymer electrolyte. and solid polymer electrolyte.[24,143,203] In the early stages, substantial research efforts were dedicated to eliminating the thermodynamic restrictions and searching for a solid-state proton-conducting electrolyte that could be operated at high temperature but atmospheric pressure. Since $SrCe_{0.95}Yb_{0.5}O_3$ had been successfully applied in ammonia synthesis at atmospheric pressure,[145] a series of solid-state electrolytes were explored to improve the ammonia synthesis rate, such as $La_{1.9}Ca_{0.1}Zr_2O_{6.95}$,[204] $BaCe_{0.85}Y_{0.15}O_{3-\alpha}$,[205] and $Ce_{0.2}M_{0.2}O_{2-\delta}$ (M = La, Y, Gd, Sm).[206]

With the development of the ammonia electrochemical conversion process, the researchers' attention has turned to the aqueous electrolyte, which they hope can achieve ammonia synthesis in the ambient environment.[207] The most common aqueous electrolytes include alkaline electrolytes (KOH,[208] $KHCO_3$[25]), acidic electrolytes (HCl, H_2SO_4), and neutral electrolytes (Li_2SO_4,[209] $LiClO_4$[140]). Among these aqueous electrolytes, the Li-mediated electrolytes have been regarded as promising electrolytes due to the enhanced interactions between Li^+ and N_2.[21,210,211] This pioneering work concluded that Li^+ is more efficient than Na^+ for N_2 adsorption, because the presence of core electrons in large cations limits the stabilizing contribution of the electrostatic and induction terms to the total energy.[194] Hans Mikosch et al. also confirmed that the adsorption energies for N_2 decrease in the order $Ca^{2+} > Na^+ > Li^+$.[195] Recently, Chen et al. used the Li^+-incorporation strategy, resulting in sluggish kinetics and a higher energy barrier for H_2 formation, but also providing appropriate NRR sites.[209] Song et al. used $LiClO_4$ for the electrochemical conversion of ammonia, because, compared to $NaClO_4$ and $KClO_4$ electrolytes, the $LiClO_4$ exhibited the highest Faradaic efficiency and yield rate due to the enhanced interactions between Li^+ and N_2.[21]

In consideration of the presence of the water, the HER side-reaction is regarded as the main reason for low Faradaic efficiency in the aqueous electrolytes employed.

© 2021 Wiley-VCH GmbH

23669608, 2021, 11, Downloaded from https://onlinelibrary.wiley.com/doi/10.1002/smtd.202100460 by University Town Of Shenzhen, Wiley Online Library on [26/11/2025]. See the Terms and Conditions (https://onlinelibrary.wiley.com/terms-and-conditions) on Wiley Online Library for rules of use; OA articles are governed by the applicable Creative Commons License

5. Conclusion and Outlook

5.1. Open Up a New Way to NH_3 Synthesis

Within the published literature, the electrochemical synthesis of N_2 and H_2O to NH_3 under ambient conditions is emerging as a most promising alternative to the H–B process among the aforementioned four kinds of NH_3 synthesis methods. The high dissociation energy of 945 kJ mol^{-1} for N≡N bonds, however, makes the N_2 molecule very stable.[212] The low yield rate and low Faradaic efficiency of the N_2 fixation process in an aqueous solution are mainly because of the difficult activation of N_2 and the competitive HER. Although theoretical analysis and experimental results have demonstrated that the occupied and unoccupied *p* states of B atoms can prohibit the binding of Lewis acid and H^+, which can circumvent the HER and promote the NRR,[173,175,213,214] the NRR process still has insufficient efficiency. Importantly, another root of the problem is the low water solubility of N_2 ($K_H = 6.24 \times 10^{-4}$ mol L^{-1} atm^{-1}).[215] Thus, seeking accessible nitrogenous species or searching for an alternative and efficient NH_3 synthesis pathway is highly promising but challenging.

Several alternative methods to the electrochemical synthesis NH_3 have been proposed. The NH_3 synthesis process can be achieved over transition metal nitrides (TMNs) via the MvK mechanism.[51] The NH_3 can be synthesized using the lattice N in TMNs, and the lattice vacancies can be further replenished with gaseous N_2.[50,74] Such an MvK strategy provides another alternative to the participation of nitrogenous species in the NRR reaction. The N_2 reduction method must be conducted, however, to demonstrate the origins of the produced ammonia origins, and the TMN-based catalyst may incur decomposition during the catalytic process.

Another alternative pathway to NH_3 synthesis is to electrochemically reduce nitrates to ammonia (NtrRR), which can use the extensive nitrates from industrial wastewater or domestic sewage.[53,216] In contrast to N_2, the nitrate salts are soluble in water and promote the mass transfer during the reaction process. Such NtrRR pathways can also greatly increase the ammonia yield rate by two or three orders of magnitude.[50,78] The Faradaic efficiency of NtrRR is nearly 100%.[36] Besides the MvK and NtrRR pathways, the metal–N_2 rechargeable batteries provides another method to produce NH_3 in spite of some intractable problems that still exist in such reversible energy-storage systems.[22,217,218] In addition, Li et al also proposed a new pathway, which active the N_2 to NO_x via plasma technique and convers the NO_x to NH_3.[219]

5.2. Boost Efficient NH_3 Synthesis by Theoretical Studies

Although recent years have witnessed a blossoming interest in the development of the electrocatalytic conversion of N_2 to NH_3, the design of the catalyst is still largely a trial-and-error process. Thus, catalyst design by the theories of constructivism is extremely important. Theoretical studies have been proven to be a powerful tool in this electrochemical synthesis of NH_3. They not only predict the most promising catalysts via computational screening, but also provide the reaction pathways via thermodynamic analysis over different catalysts for better understanding of the reaction mechanism.[67–69,74,91] Based on the free energy of intermediates found by DFT calculations, volcano plots relating to the NRR activity of different catalysts have been constructed, which provide theoretical guidance toward the selection and optimization of electrocatalysts. [86,220,221] In addition, the electronic structure analysis between the catalyst and the intermediates, such as for the density of states (DOS), spin density, and charge density also provides strong evidence to aid in the investigation of mechanisms.[222] With the development of in situ technology, such as in situ Raman, in situ FTIR, online differential electrochemical mass spectrometry (DEMS), which can determine the electrochemical reaction intermediates. The combination of advanced online characterization and theoretical study accelerates the understanding of the reaction pathway.[223]

5.3. Improve the Activity and Selectivity of the NRR

Research on the electrochemical synthesis of NH_3 has seen much progress in recent years, as evidenced by the rapidly increasing number of publications on this subject, but the major challenges are the limited yield rate and low Faradaic efficiency resulting from the higher N_2 activation barrier and the competing HER reaction. To improve the activity and selectivity during the electrochemical NH_3 synthesis process, in this review, some strategies have been summarized. One important strategy is to rationally design highly effective and selective catalysts, which can expose more active sites, possess binding energy with N or intermediates, and simultaneously suppress the competing HER reaction. The advanced design strategies, such as the introduction of defects, heteroatom doping, crystal-facet design, and alloying, could tune the physicochemical properties on the atomic level, improve the affinity of N-adatoms, and further enhance the catalytic activity.

Besides the rational design of the catalyst, advanced electrocatalytic systems should be considering for suppressing the HER reaction. The optimization of the interfaces between the electrolyte and the cathode, such as using MEA technology, can prevent H_2O access to the cathode. The addition of 2-propanol can suppress the HER, and the Li^+-incorporation strategy can increase the solubility of N_2.[21]

5.4. Optimize the Measurement of Ammonia

Up to now, a series of measurement methods have been used for ammonia detection, such as ion-selective electrodes (ISEs), ion chromatography, the colorimetric method (including indophenol blue, salicylate acid, the phenate method, and Nessler's reagent method), and enzymatic testing. However, the amount of ammonia produced is usually as low as the nanomole level, it cannot be firmly attributed to the nitrogen electroreduction process. Both out-system and intrasystem may contain the contamination source, such as the NH_3, NO_x in the air or human breath, nitrogen-containing compounds in the electrocatalyst or electrolyte.[224] It is difficult to completely rule out the contribution of NH_3 derived from N-based

© 2021 Wiley-VCH GmbH

23669608, 2021, 11, Downloaded from https://onlinelibrary.wiley.com/doi/10.1002/smtd.202100460 by University Town Of Shenzhen, Wiley Online Library on [26/11/2025]. See the Terms and Conditions (https://onlinelibrary.wiley.com/terms-and-conditions) on Wiley Online Library for rules of use; OA articles are governed by the applicable Creative Commons License

materials or N-containing electrolytes,[225] and the synthesized ammonia in the cathode may cross over the Nafion membrane to be oxidized in the anode, accurate and reliable measurements of the ammonia have been limited.[226] Therefore, to clarify the source of ammonia and accurately measure the amount of ammonia, a protocol for rigorous experimentation must be proposed.

- As the existence of NO_x in the electrolyte could cause significant false positive results. The prejudgment of NO_x^- in the electrolyte is strongly recommended prior to NRR. Running the NRR test under Ar gas is necessary and the impurity in the electrolyte can be effectively removed by high-temperature treatment.
- Because the spectroscopic assays can be influenced by the solution conditions. The isotopic labeling experiments ($^{15}N_2$) should be performed. Before the labeling experiment, the $^{15}N_2$ gas should be treated with sulfuric acid overnight to remove the $^{15}NH_4^+$, $^{15}NO_2^-$, and other impurities.[224] Moreover, to obtain reliable and reproducible results, the error bars are suggested to be included in repeated runs of NRR testing.
- The nitrogen-containing compounds in the electrocatalyst may lead to false positive result, typically metal nitride. Thus, mass spectroscopy and NMR are suggested to verify the source of nitrogen.

Acknowledgements

Y.L. and Q.Z. contributed equally to this work. This work was supported by Australian Research Council (ARC) DP160102627, ARC DP170101467, and ARC-LIEF Grants (LE120100104 and LE0237478), as well as the China Scholarship Council (CSC). The authors also would like to acknowledge the financial support from the Shenzhen Science and Technology Research Grant (JCYJ20200109140416788), the Chemistry and Chemical Engineering Guangdong Laboratory (Grant No.1922018) and National Key R&D Program of China (2020YFB0704500). Dr. Tania Silver is thanked for critical reading of the manuscript. This manuscript was written through the contributions of all the authors. All the authors have given approval to the final version of the manuscript.

Conflict of Interest

The authors declare no conflict of interest.

Keywords

electrocatalysis, electrochemical ammonia synthesis, material design strategies, reaction mechanisms

Received: April 27, 2021
Revised: August 15, 2021
Published online: September 17, 2021

[1] J. W. Erisman, M. A. Sutton, J. Galloway, Z. Klimont, W. Winiwarter, *Nat. Geosci.* **2008**, *1*, 636.
[2] G. F. Chen, S. Ren, L. Zhang, H. Cheng, Y. Luo, K. Zhu, L. X. Ding, H. Wang, *Small Methods* **2019**, *3*, 1800337.
[3] L. Wang, M. Xia, H. Wang, K. Huang, C. Qian, C. T. Maravelias, G. A. Ozin, *Joule* **2018**, *2*, 1055.
[4] C. Tang, S.-Z. Qiao, *Chem. Soc. Rev.* **2019**, *48*, 3166.
[5] H. Liu, L. Wei, F. Liu, Z. Pei, J. Shi, Z.-j. Wang, D. He, Y. Chen, *ACS Catal.* **2019**, *9*, 5245.
[6] M. Kitano, Y. Inoue, Y. Yamazaki, F. Hayashi, S. Kanbara, S. Matsuishi, T. Yokoyama, S.-W. Kim, M. Hara, H. Hosono, *Nat. Chem.* **2012**, *4*, 934.
[7] J. G. Chen, R. M. Crooks, L. C. Seefeldt, K. L. Bren, R. M. Bullock, M. Y. Darensbourg, P. L. Holland, B. Hoffman, M. J. Janik, A. K. Jones, *Science* **2018**, *360*, eaar6611.
[8] C. Liu, K. K. Sakimoto, B. C. Colón, P. A. Silver, D. G. Nocera, *Proc. Natl. Acad. Sci. USA* **2017**, *114*, 6450.
[9] T. Spatzal, K. A. Perez, O. Einsle, J. B. Howard, D. C. Rees, *Science* **2014**, *345*, 1620.
[10] D. V. Yandulov, R. R. Schrock, *Science* **2003**, *301*, 76.
[11] K. Tanifuji, N. Sickerman, C. C. Lee, T. Nagasawa, K. Miyazaki, Y. Ohki, K. Tatsumi, Y. Hu, M. W. Ribbe, *Angew. Chem., Int. Ed.* **2016**, *55*, 15633.
[12] I. Čorić, B. Q. Mercado, E. Bill, D. J. Vinyard, P. L. Holland, *Nature* **2015**, *526*, 96.
[13] S. L. Foster, S. I. P. Bakovic, R. D. Duda, S. Maheshwari, R. D. Milton, S. D. Minteer, M. J. Janik, J. N. Renner, L. F. Greenlee, *Nat. Catal.* **2018**, *1*, 490.
[14] J. S. Anderson, J. Rittle, J. C. Peters, *Nature* **2013**, *501*, 84.
[15] R. R. Schrock, *Acc. Chem. Res.* **2005**, *38*, 955.
[16] M. M. Rodriguez, E. Bill, W. W. Brennessel, P. L. Holland, *Science* **2011**, *334*, 780.
[17] T. Oshikiri, K. Ueno, H. Misawa, *Angew. Chem., Int. Ed.* **2016**, *128*, 4010.
[18] R. F. Service, *Science* **2014**, *345*, 610.
[19] C. J. Pickett, J. Talarmin, *Nature* **1985**, *317*, 652.
[20] J. N. Renner, L. F. Greenlee, K. E. Ayres, A. M. Herring, *Electrochem. Soc. Interface* **2015**, *24*, 51.
[21] Y. Song, D. Johnson, R. Peng, D. K. Hensley, P. V. Bonnesen, L. Liang, J. Huang, F. Yang, F. Zhang, R. Qiao, *Sci. Adv.* **2018**, *4*, e1700336.
[22] A. Singh, B. Rohr, *Energy Environ. Sci.* **2017**, *10*, 1621.
[23] J.-L. Ma, D. Bao, M.-M. Shi, J.-M. Yan, X.-B. Zhang, *Chem* **2017**, *2*, 525.
[24] V. Kordali, G. Kyriacou, C. Lambrou, *Chem. Commun.* **2000**, *2000*, 1673.
[25] S. Chen, S. Perathoner, C. Ampelli, C. Mebrahtu, D. Su, G. Centi, *Angew. Chem., Int. Ed.* **2017**, *56*, 2699.
[26] D. Bao, Q. Zhang, F. L. Meng, H. X. Zhong, M. M. Shi, Y. Zhang, J. M. Yan, Q. Jiang, X. B. Zhang, *Adv. Mater.* **2017**, *29*, 1604799.
[27] D. Yang, T. Chen, Z. Wang, *J. Mater. Chem. A* **2017**, *5*, 18967.
[28] S. Licht, B. Cui, B. Wang, F.-F. Li, J. Lau, S. Liu, *Science* **2014**, *345*, 637.
[29] J. Han, X. Ji, X. Ren, G. Cui, L. Li, F. Xie, H. Wang, B. Li, X. Sun, *J. Mater. Chem. A* **2018**, *6*, 12974.
[30] B. H. Suryanto, D. Wang, L. M. Azofra, M. Harb, L. Cavallo, R. Jalili, D. R. Mitchell, M. Chatti, D. R. MacFarlane, *ACS Energy Lett.* **2018**, *4*, 430.
[31] K. Chu, Q.-q. Li, Y.-h. Cheng, Y.-p. Liu, *ACS Appl. Mater. Interfaces* **2020**, *12*, 11789.
[32] Q. Liu, X. Zhang, J. Wang, Y. Zhang, S. Bian, Z. Cheng, N. Kang, H. Huang, S. Gu, Y. Wang, *Angew. Chem., Int. Ed.* **2020**, *59*, 14383.
[33] C. H. Choi, S. H. Park, S. I. Woo, *ACS Nano* **2012**, *6*, 7084.
[34] H. B. Yang, J. Miao, S.-F. Hung, J. Chen, H. B. Tao, X. Wang, L. Zhang, R. Chen, J. Gao, H. M. Chen, *Sci. Adv.* **2016**, *2*, e1501122.
[35] B. Liu, Y. Zheng, H.-Q. Peng, B. Ji, Y. Yang, Y. Tang, C.-S. Lee, W. Zhang, *ACS Energy Lett.* **2020**, *5*, 2590.
[36] Y. Wang, W. Zhou, R. Jia, Y. Yu, B. Zhang, *Angew. Chem., Int. Ed.* **2020**, *132*, 5388.
[37] X. Li, K. Lu, *Nat. Mater.* **2017**, *16*, 700.

 © 2021 Wiley-VCH GmbH

23669608, 2021, 11, Downloaded from https://onlinelibrary.wiley.com/doi/10.1002/smtd.202100460 by University Town Of Shenzhen, Wiley Online Library on [26/11/2025]. See the Terms and Conditions (https://onlinelibrary.wiley.com/terms-and-conditions) on Wiley Online Library for rules of use; OA articles are governed by the applicable Creative Commons License

[38] M. Asano, R. Kawamura, R. Sasakawa, N. Todoroki, T. Wadayama, *ACS Catal.* **2016**, *6*, 5285.
[39] R. Lin, J. Wan, Y. Xiong, K. Wu, W.-c. Cheong, G. Zhou, D. Wang, Q. Peng, C. Chen, Y. Li, *J. Am. Chem. Soc.* **2018**, *140*, 9078.
[40] R. Li, F. Zhang, D. Wang, J. Yang, M. Li, J. Zhu, X. Zhou, H. Han, C. Li, *Nat. Commun.* **2013**, *4*, 1.
[41] Y. Jia, L. Zhang, A. Du, G. Gao, J. Chen, X. Yan, C. L. Brown, X. Yao, *Adv. Mater.* **2016**, *28*, 9532.
[42] D. Sangiovanni, A. Mei, L. Hultman, V. Chirita, I. Petrov, J. E. Greene, *J. Phys. Chem. C* **2016**, *120*, 12503.
[43] Q. Wang, Y. Lei, D. Wang, Y. Li, *Energy Environ. Sci.* **2019**, *12*, 1730.
[44] X. X. Wang, D. A. Cullen, Y. T. Pan, S. Hwang, M. Wang, Z. Feng, J. Wang, M. H. Engelhard, H. Zhang, Y. He, *Adv. Mater.* **2018**, *30*, 1706758.
[45] J. Zhang, J. Liu, L. Xi, Y. Yu, N. Chen, S. Sun, W. Wang, K. M. Lange, B. Zhang, *J. Am. Chem. Soc.* **2018**, *140*, 3876.
[46] Q. Feng, S. Zhao, Y. Wang, J. Dong, W. Chen, D. He, D. Wang, J. Yang, Y. Zhu, H. Zhu, *J. Am. Chem. Soc.* **2017**, *139*, 7294.
[47] W. Sun, R. Shi, X. Wang, S. Liu, X. Han, C. Zhao, Z. Li, J. Ren, *Appl. Surf. Sci.* **2017**, *425*, 291.
[48] H. Zhang, G. Liu, L. Shi, J. Ye, *Adv. Energy Mater.* **2018**, *8*, 1701343.
[49] Y. Chen, S. Ji, Y. Wang, J. Dong, W. Chen, Z. Li, R. Shen, L. Zheng, Z. Zhuang, D. Wang, *Angew. Chem., Int. Ed.* **2017**, *56*, 6937.
[50] Y. Abghoui, A. L. Garden, V. F. Hlynsson, S. Björgvinsdóttir, H. Ólafsdóttir, E. Skúlason, *Phys. Chem. Chem. Phys.* **2015**, *17*, 4909.
[51] Y. Abghoui, E. Skúlason, *Catal. Today* **2017**, *286*, 69.
[52] B. Hu, M. Hu, L. Seefeldt, T. L. Liu, *ACS Energy Lett.* **2019**, *4*, 1053.
[53] X. Fu, X. Zhao, X. Hu, K. He, Y. Yu, T. Li, Q. Tu, X. Qian, Q. Yue, M. R. Wasielewski, *Appl. Mater. Today* **2020**, *19*, 100620.
[54] G.-F. Chen, Y. Yuan, H. Jiang, S.-Y. Ren, L.-X. Ding, L. Ma, T. Wu, J. Lu, H. Wang, *Nat. Energy* **2020**, *5*, 605.
[55] P. H. van Langevelde, I. Katsounaros, M. T. Koper, *Joule* **2021**, *5*, 290.
[56] R. Jia, Y. Wang, C. Wang, Y. Ling, Y. Yu, B. Zhang, *ACS Catal.* **2020**, *10*, 3533.
[57] L. Wei, D.-J. Liu, B. A. Rosales, J. W. Evans, J. Vela, *ACS Catal.* **2020**, *10*, 3618.
[58] H. Wang, Z. Li, Y. Li, B. Yang, J. Chen, L. Lei, S. Wang, Y. Hou, *Nano Energy* **2021**, *81*, 105613.
[59] B. Ge, Y. Wang, Y. Sun, Y. Li, J. Huang, Q. Peng, *Energy Storage Mater.* **2019**, *23*, 733.
[60] Y. Zeng, C. Priest, G. Wang, G. Wu, *Small Methods* **2020**, *4*, 2000672.
[61] J. B. Howard, D. C. Rees, *Chem. Rev.* **1996**, *96*, 2965.
[62] S. Raugei, L. C. Seefeldt, B. M. Hoffman, *Proc. Natl. Acad. Sci. USA* **2018**, *115*, E10521.
[63] J. Chatt, J. R. Dilworth, R. L. Richards, *Chem. Rev.* **1978**, *78*, 589.
[64] Y. Yao, H. Wang, X.-z. Yuan, H. Li, M. Shao, *ACS Energy Lett.* **2019**, *4*, 1336.
[65] E. Skulason, T. Bligaard, S. Gudmundsdóttir, F. Studt, J. Rossmeisl, F. Abild-Pedersen, T. Vegge, H. Jónsson, J. K. Nørskov, *Phys. Chem. Chem. Phys.* **2012**, *14*, 1235.
[66] C. J. Van der Ham, M. T. Koper, D. G. Hetterscheid, *Chem. Soc. Rev.* **2014**, *43*, 5183.
[67] A. Logadottir, J. K. Nørskov, *J. Catal.* **2003**, *220*, 273.
[68] S. Dahl, A. Logadottir, R. Egeberg, J. Larsen, I. Chorkendorff, E. Törnqvist, J. K. Nørskov, *Phys. Rev. Lett.* **1999**, *83*, 1814.
[69] T. H. Rod, A. Logadottir, J. K. Nørskov, *J. Chem. Phys.* **2000**, *112*, 5343.
[70] M. A. Shipman, M. D. Symes, *Catal. Today* **2017**, *286*, 57.
[71] A. Shilov, *Russ. Chem. Bull.* **2003**, *52*, 2555.
[72] C. T. Bazhenova, A. Shilov, *Coord. Chem. Rev.* **1995**, *144*, 69.
[73] N. Shan, V. Chikan, P. Pfromm, B. Liu, *J. Phys. Chem. C* **2018**, *122*, 6109.
[74] Y. Abghoui, A. L. Garden, J. G. Howalt, T. Vegge, E. Skúlason, *ACS Catal.* **2016**, *6*, 635.
[75] A. W. Tricker, K. L. Hebisch, M. Buchmann, Y.-H. Liu, M. Rose, E. Stavitski, A. J. Medford, M. C. Hatzell, C. Sievers, *ACS Energy Lett.* **2020**, *5*, 3362.
[76] Q. Li, L. He, C. Sun, X. Zhang, *J. Phys. Chem. C* **2017**, *121*, 27563.
[77] J. Choi, H.-L. Du, C. K. Nguyen, B. H. Suryanto, A. N. Simonov, D. R. MacFarlane, *ACS Energy Lett.* **2020**, *5*, 2095.
[78] J. Li, G. Zhan, J. Yang, F. Quan, C. Mao, Y. Liu, B. Wang, F. Lei, L. Li, A. W. Chan, *J. Am. Chem. Soc.* **2020**, *142*, 7036.
[79] Z.-Y. Wu, M. Karamad, X. Yong, Q. Huang, D. A. Cullen, P. Zhu, C. Xia, Q. Xiao, M. Shakouri, F.-Y. Chen, *Nat. Commun.* **2021**, *12*, 2870.
[80] J. M. McEnaney, S. J. Blair, A. C. Nielander, J. A. Schwalbe, D. M. Koshy, M. Cargnello, T. F. Jaramillo, *ACS Sustainable Chem. Eng.* **2020**, *8*, 2672.
[81] C. Y. Su, H. Cheng, W. Li, Z. Q. Liu, N. Li, Z. Hou, F. Q. Bai, H. X. Zhang, T. Y. Ma, *Adv. Energy Mater.* **2017**, *7*, 1602420.
[82] Y. Guo, Q. Yang, D. Wang, H. Li, Z. Huang, X. Li, Y. Zhao, B. Dong, C. Zhi, *Energy Environ. Sci.* **2020**, *13*, 2888.
[83] Z. Seh, J. Kibsgaard, C. Dickens, I. Chorkendorff, J. Norskov, T. Jaramillo, *Science* **2017**, *355*, eaad4998.
[84] A. Logadottir, T. H. Rod, J. K. Nørskov, B. Hammer, S. Dahl, C. Jacobsen, *J. Catal.* **2001**, *197*, 229.
[85] S. Zheng, S. Li, Z. Mei, Z. Hu, M. Chu, J. Liu, X. Chen, F. Pan, *J. Phys. Chem. Lett.* **2019**, *10*, 6984.
[86] A. J. Medford, A. Vojvodic, J. S. Hummelshøj, J. Voss, F. Abild-Pedersen, F. Studt, T. Bligaard, A. Nilsson, J. K. Nørskov, *J. Catal.* **2015**, *328*, 36.
[87] J. Pérez-Ramírez, N. López, *Nat. Catal.* **2019**, *2*, 971.
[88] Y.-C. Hao, Y. Guo, L.-W. Chen, M. Shu, X.-Y. Wang, T.-A. Bu, W.-Y. Gao, N. Zhang, X. Su, X. Feng, *Nat. Catal.* **2019**, *2*, 448.
[89] P. Wang, F. Chang, W. Gao, J. Guo, G. Wu, T. He, P. Chen, *Nat. Chem.* **2017**, *9*, 64.
[90] J. H. Montoya, C. Tsai, A. Vojvodic, J. K. Nørskov, *ChemSusChem* **2015**, *8*, 2180.
[91] A.r.B. Höskuldsson, Y. Abghoui, A. B. Gunnarsdóttir, E. Skúlason, *ACS Sustainable Chem. Eng.* **2017**, *5*, 10327.
[92] Y. Abghoui, E. Skúlason, *Catal. Today* **2017**, *286*, 78.
[93] X. Hu, Y. Sun, S. Guo, J. Sun, Y. Fu, S. Chen, S. Zhang, J. Zhu, *Appl. Catal., B* **2021**, *280*, 119419.
[94] J. Han, Z. Liu, Y. Ma, G. Cui, F. Xie, F. Wang, Y. Wu, S. Gao, Y. Xu, X. Sun, *Nano Energy* **2018**, *52*, 264.
[95] C. Lv, C. Yan, G. Chen, Y. Ding, J. Sun, Y. Zhou, G. Yu, *Angew. Chem., Int. Ed.* **2018**, *130*, 6181.
[96] X. Han, C. S. Gerke, S. Banerjee, M. Zubair, J. Jiang, N. M. Bedford, E. M. Miller, V. S. Thoi, *ACS Energy Lett.* **2020**, *5*, 3237.
[97] L. Zhang, X. Ji, X. Ren, Y. Luo, X. Shi, A. M. Asiri, B. Zheng, X. Sun, *ACS Sustainable Chem. Eng.* **2018**, *6*, 9550.
[98] I. A. Amar, R. Lan, C. T. Petit, S. Tao, *Int. J. Electrochem. Sci.* **2015**, *10*, 3757.
[99] H. Wang, X. Xiao, S. Liu, C.-L. Chiang, X. Kuai, C.-K. Peng, Y.-C. Lin, X. Meng, J. Zhao, J. Choi, *J. Am. Chem. Soc.* **2019**, *141*, 18578.
[100] N. Furuya, H. Yoshiba, *J. Electroanal. Chem.* **1990**, *291*, 269.
[101] W. Zhang, K. Mao, J. Low, H. Liu, Y. Bo, J. Ma, Q. Liu, Y. Jiang, J. Yang, Y. Pan, *Nano Res.* **2021**, *14*, 3234.
[102] Y. Liu, Y. Su, X. Quan, X. Fan, S. Chen, H. Yu, H. Zhao, Y. Zhang, J. Zhao, *ACS Catal.* **2018**, *8*, 1186.
[103] Y. Luo, G.-F. Chen, L. Ding, X. Chen, L.-X. Ding, H. Wang, *Joule* **2019**, *3*, 279.
[104] G. Xu, H. Li, A. S. Bati, M. Bat-Erdene, M. J. Nine, D. Losic, Y. Chen, J. G. Shapter, M. Batmunkh, T. Ma, *J. Mater. Chem. A* **2020**, *8*, 15875.
[105] L. Li, C. Tang, B. Xia, H. Jin, Y. Zheng, S.-Z. Qiao, *ACS Catal.* **2019**, *9*, 2902.
[106] M. Bat-Erdene, G. Xu, M. Batmunkh, A. S. Bati, J. J. White, M. J. Nine, D. Losic, Y. Chen, Y. Wang, T. Ma, *J. Mater. Chem. A* **2020**, *8*, 4735.

 © 2021 Wiley-VCH GmbH

23669608, 2021, 11, Downloaded from https://onlinelibrary.wiley.com/doi/10.1002/smtd.202100460 by University Town Of Shenzhen, Wiley Online Library on [26/11/2025]. See the Terms and Conditions (https://onlinelibrary.wiley.com/terms-and-conditions) on Wiley Online Library for rules of use; OA articles are governed by the applicable Creative Commons License

[107] L. X. Chen, Z. W. Chen, M. Jiang, Z. Lu, C. Gao, G. Cai, C. V. Singh, *J. Mater. Chem. A* **2021**, *9*, 2018.
[108] C. Lv, Y. Qian, C. Yan, Y. Ding, Y. Liu, G. Chen, G. Yu, *Angew. Chem., Int. Ed.* **2018**, *130*, 10403.
[109] H. Wang, L. Wang, Q. Wang, S. Ye, W. Sun, Y. Shao, Z. Jiang, Q. Qiao, Y. Zhu, P. Song, *Angew. Chem., Int. Ed.* **2018**, *57*, 12360.
[110] X. Yu, P. Han, Z. Wei, L. Huang, Z. Gu, S. Peng, J. Ma, G. Zheng, *Joule* **2018**, *2*, 1610.
[111] W. Qiu, X.-Y. Xie, J. Qiu, W.-H. Fang, R. Liang, X. Ren, X. Ji, G. Cui, A. M. Asiri, G. Cui, *Nat. Commun.* **2018**, *9*, 1.
[112] Y. Liu, Q. Li, X. Guo, X. Kong, J. Ke, M. Chi, Q. Li, Z. Geng, J. Zeng, *Adv. Mater.* **2020**, *32*, 1907690.
[113] D. Yuan, Z. Wei, P. Han, C. Yang, L. Huang, Z. Gu, Y. Ding, J. Ma, G. Zheng, *J. Mater. Chem. A* **2019**, *7*, 16979.
[114] L. Zhang, L. X. Ding, G. F. Chen, X. Yang, H. Wang, *Angew. Chem., Int. Ed.* **2019**, *58*, 2612.
[115] X. Zhang, T. Wu, H. Wang, R. Zhao, H. Chen, T. Wang, P. Wei, Y. Luo, Y. Zhang, X. Sun, *ACS Catal.* **2019**, *9*, 4609.
[116] S. Liu, M. Wang, T. Qian, H. Ji, J. Liu, C. Yan, *Nat. Commun.* **2019**, *10*, 3898.
[117] Y. Li, Q. Zhang, C. Li, H.-N. Fan, W.-B. Luo, H.-K. Liu, S.-X. Dou, *J. Mater. Chem. A* **2019**, *7*, 22242.
[118] L. Han, X. Liu, J. Chen, R. Lin, H. Liu, F. Lü, S. Bak, Z. Liang, S. Zhao, E. Stavitski, *Angew. Chem., Int. Ed.* **2019**, *58*, 2321.
[119] L. Hui, Y. Xue, H. Yu, Y. Liu, Y. Fang, C. Xing, B. Huang, Y. Li, *J. Am. Chem. Soc.* **2019**, *141*, 10677.
[120] S. Zhang, M. Jin, T. Shi, M. Han, Q. Sun, Y. Lin, Z. Ding, L. R. Zheng, G. Wang, Y. Zhang, *Angew. Chem., Int. Ed.* **2020**, *132*, 13525.
[121] C. He, Z.-Y. Wu, L. Zhao, M. Ming, Y. Zhang, Y. Yi, J.-S. Hu, *ACS Catal.* **2019**, *9*, 7311.
[122] F. Lü, S. Zhao, R. Guo, J. He, X. Peng, H. Bao, J. Fu, L. Han, G. Qi, J. Luo, *Nano Energy* **2019**, *61*, 420.
[123] J. Li, S. Chen, F. Quan, G. Zhan, F. Jia, Z. Ai, L. Zhang, *Chem* **2020**, *6*, 885.
[124] M. Wang, S. Liu, T. Qian, J. Liu, J. Zhou, H. Ji, J. Xiong, J. Zhong, C. Yan, *Nat. Commun.* **2019**, *10*, 341.
[125] B. Yu, H. Li, J. White, S. Donne, J. Yi, S. Xi, Y. Fu, G. Henkelman, H. Yu, Z. Chen, *Adv. Funct. Mater.* **2020**, *30*, 1905665.
[126] H. Tao, C. Choi, L.-X. Ding, Z. Jiang, Z. Han, M. Jia, Q. Fan, Y. Gao, H. Wang, A. W. Robertson, *Chem* **2019**, *5*, 204.
[127] Z. Geng, Y. Liu, X. Kong, P. Li, K. Li, Z. Liu, J. Du, M. Shu, R. Si, J. Zeng, *Adv. Mater.* **2018**, *30*, 1803498.
[128] Q. Qin, T. Heil, M. Antonietti, M. Oschatz, *Small Methods* **2018**, *2*, 1800202.
[129] X. Wang, W. Wang, M. Qiao, G. Wu, W. Chen, T. Yuan, Q. Xu, M. Chen, Y. Zhang, X. Wang, *Sci. Bull.* **2018**, *63*, 1246.
[130] S. Mukherjee, X. Yang, W. Shan, W. Samarakoon, S. Karakalos, D. A. Cullen, K. More, M. Wang, Z. Feng, G. Wang, *Small Methods* **2020**, *4*, 1900821.
[131] J. Zhang, X. Tian, M. Liu, H. Guo, J. Zhou, Q. Fang, Z. Liu, Q. Wu, J. Lou, *J. Am. Chem. Soc.* **2019**, *141*, 19269.
[132] X. Xiang, Z. Wang, X. Shi, M. Fan, X. Sun, *ChemCatChem* **2018**, *10*, 4530.
[133] S. Chen, S. Perathoner, C. Ampelli, H. Wei, S. Abate, B. Zhang, G. Centi, *J. Energy Chem.* **2020**, *49*, 22.
[134] X. Cui, C. Tang, X. M. Liu, C. Wang, W. Ma, Q. Zhang, *Chem. - Eur. J.* **2018**, *24*, 18494.
[135] R. Zhang, X. Ren, X. Shi, F. Xie, B. Zheng, X. Guo, X. Sun, *ACS Appl. Mater. Interfaces* **2018**, *10*, 28251.
[136] X. Zhang, R.-M. Kong, H. Du, L. Xia, F. Qu, *Chem. Commun.* **2018**, *54*, 5323.
[137] W. Guo, Z. Liang, J. Zhao, B. Zhu, K. Cai, R. Zou, Q. Xu, *Small Methods* **2018**, *2*, 1800204.
[138] M. M. Shi, D. Bao, B. R. Wulan, Y. H. Li, Y. F. Zhang, J. M. Yan, Q. Jiang, *Adv. Mater.* **2017**, *29*, 1606550.
[139] S. J. Li, D. Bao, M. M. Shi, B. R. Wulan, J. M. Yan, Q. Jiang, *Adv. Mater.* **2017**, *29*, 1700001.
[140] M. Nazemi, S. R. Panikkanvalappil, M. A. El-Sayed, *Nano Energy* **2018**, *49*, 316.
[141] H.-M. Liu, S.-H. Han, Y. Zhao, Y.-Y. Zhu, X.-L. Tian, J.-H. Zeng, J.-X. Jiang, B. Y. Xia, Y. Chen, *J. Mater. Chem. A* **2018**, *6*, 3211.
[142] R. Lan, S. Tao, *RSC Adv.* **2013**, *3*, 18016.
[143] B. L. Sheets, G. G. Botte, *Chem. Commun.* **2018**, *54*, 4250.
[144] K. Kugler, M. Luhn, J. A. Schramm, K. Rahimi, M. Wessling, *Phys. Chem. Chem. Phys.* **2015**, *17*, 3768.
[145] G. Marnellos, M. Stoukides, *Science* **1998**, *282*, 98.
[146] K. Kim, C.-Y. Yoo, J.-N. Kim, H. C. Yoon, J.-I. Han, *J. Electrochem. Soc.* **2016**, *163*, F1523.
[147] A. Tsuneto, A. Kudo, T. Sakata, *J. Eleectroanal. Chem.* **1994**, *367*, 183.
[148] R. Lan, J. T. Irvine, S. Tao, *Sci. Rep.* **2013**, *3*, 1.
[149] F. Pang, Z. Wang, K. Zhang, J. He, W. Zhang, C. Guo, Y. Ding, *Nano Energy* **2019**, *58*, 834.
[150] M. M. Shi, D. Bao, S. J. Li, B. R. Wulan, J. M. Yan, Q. Jiang, *Adv. Energy Mater.* **2018**, *8*, 1800124.
[151] R. Manjunatha, A. Schechter, *Electrochem. Commun.* **2018**, *90*, 96.
[152] H. Wang, Y. Li, D. Yang, X. Qian, Z. Wang, Y. Xu, X. Li, H. Xue, L. Wang, *Nanoscale* **2019**, *11*, 5499.
[153] X. Fan, Y. Liu, S. Chen, J. Shi, J. Wang, A. Fan, W. Zan, S. Li, W. A. Goddard, X.-M. Zhang, *Nat. Commun.* **2018**, *9*, 1809.
[154] J. Xie, H. Zhang, S. Li, R. Wang, X. Sun, M. Zhou, J. Zhou, X. W. Lou, Y. Xie, *Adv. Mater.* **2013**, *25*, 5807.
[155] L. Tao, Q. Wang, S. Dou, Z. Ma, J. Huo, S. Wang, L. Dai, *Chem. Commun.* **2016**, *52*, 2764.
[156] H. Li, J. Shang, Z. Ai, L. Zhang, *J. Am. Chem. Soc.* **2015**, *137*, 6393.
[157] H. Hirakawa, M. Hashimoto, Y. Shiraishi, T. Hirai, *J. Am. Chem. Soc.* **2017**, *139*, 10929.
[158] Y. Zhao, Y. Zhao, G. I. Waterhouse, L. Zheng, X. Cao, F. Teng, L. Z. Wu, C. H. Tung, D. O'Hare, T. Zhang, *Adv. Mater.* **2017**, *29*, 1703828.
[159] Y. Jiao, Y. Zheng, K. Davey, S.-Z. Qiao, *Nat. Energy* **2016**, *1*, 16130.
[160] Y. Zheng, Y. Jiao, Y. Zhu, L. H. Li, Y. Han, Y. Chen, A. Du, M. Jaroniec, S. Z. Qiao, *Nat. Commun.* **2014**, *5*, 1.
[161] Y. Yang, L. Zhang, Z. Hu, Y. Zheng, C. Tang, P. Chen, R. Wang, K. Qiu, J. Mao, T. Ling, *Angew. Chem., Int. Ed.* **2020**, *59*, 4525.
[162] W. Peng, M. Luo, X. Xu, K. Jiang, M. Peng, D. Chen, T. S. Chan, Y. Tan, *Adv. Energy Mater.* **2020**, *10*, 2001364.
[163] R. Hao, W. Sun, Q. Liu, X. Liu, J. Chen, X. Lv, W. Li, Y. p. Liu, Z. Shen, *Small* **2020**, *16*, 2000015.
[164] C. Zhu, S. Fu, Q. Shi, D. Du, Y. Lin, *Angew. Chem., Int. Ed.* **2017**, *56*, 13944.
[165] Y. Lei, F. Mehmood, S. Lee, J. Greeley, B. Lee, S. Seifert, R. E. Winans, J. W. Elam, R. J. Meyer, P. C. Redfern, *Science* **2010**, *328*, 224.
[166] H. Xu, D. Cheng, D. Cao, X. C. Zeng, *Nat. Catal.* **2018**, *1*, 339.
[167] H. Fei, J. Dong, Y. Feng, C. S. Allen, C. Wan, B. Volosskiy, M. Li, Z. Zhao, Y. Wang, H. Sun, *Nat. Catal.* **2018**, *1*, 63.
[168] Z. Wang, Z. Yu, J. Zhao, *Phys. Chem. Chem. Phys.* **2018**, *20*, 12835.
[169] J. Zhao, Z. Chen, *J. Am. Chem. Soc.* **2017**, *139*, 12480.
[170] X. Liu, Y. Jiao, Y. Zheng, M. Jaroniec, S.-Z. Qiao, *J. Am. Chem. Soc.* **2019**, *141*, 9664.
[171] T. Yang, T. T. Song, J. Zhou, S. Wang, D. Chi, L. Shen, M. Yang, Y. P. Feng, *Nano Energy* **2020**, *68*, 104304.
[172] Z. Wang, X. Wu, Y. Qin, Y. Han, D. Zhang, H. Zhao, J. Chi, G. Xu, M. Wang, S. Li, *J. Mater. Chem. A* **2021**, *9*, 894.
[173] C. Hering-Junghans, *Angew. Chem., Int. Ed.* **2018**, *57*, 6738.
[174] B. Chang, L. Li, D. Shi, H. Jiang, Z. Ai, S. Wang, Y. Shao, J. Shen, Y. Wu, Y. Li, *Appl. Catal., B* **2021**, *283*, 119622.
[175] C. Liu, Q. Li, C. Wu, J. Zhang, Y. Jin, D. R. MacFarlane, C. Sun, *J. Am. Chem. Soc.* **2019**, *141*, 2884.
[176] H.-R. Zhu, Y.-L. Hu, S.-H. Wei, D.-Y. Hua, *J. Phys. Chem. C* **2019**, *123*, 4274.

 © 2021 Wiley-VCH GmbH

23669608, 2021, 11, Downloaded from https://onlinelibrary.wiley.com/doi/10.1002/smtd.202100460 by University Town Of Shenzhen, Wiley Online Library on [26/11/2025]. See the Terms and Conditions (https://onlinelibrary.wiley.com/terms-and-conditions) on Wiley Online Library for rules of use; OA articles are governed by the applicable Creative Commons License

[177] S. Zhou, X. Yang, X. Xu, S. X. Dou, Y. Du, J. Zhao, *J. Am. Chem. Soc.* **2019**, *142*, 308.
[178] X. Liu, Y. Jiao, Y. Zheng, S.-Z. Qiao, *ACS Catal.* **2020**, *10*, 1847.
[179] X. Guo, J. Gu, S. Lin, S. Zhang, Z. Chen, S. Huang, *J. Am. Chem. Soc.* **2020**, *142*, 5709.
[180] X. Lv, W. Wei, B. Huang, Y. Dai, T. Frauenheim, *Nano Lett.* **2021**, *21*, 1871.
[181] C. Deng, Y. Su, F. Li, W. Shen, Z. Chen, Q. Tang, *J. Mater. Chem. A* **2020**, *8*, 24563.
[182] H. G. Yang, C. H. Sun, S. Z. Qiao, J. Zou, G. Liu, S. C. Smith, H. M. Cheng, G. Q. Lu, *Nature* **2008**, *453*, 638.
[183] C. Chen, Y. Kang, Z. Huo, Z. Zhu, W. Huang, H. L. Xin, J. D. Snyder, D. Li, J. A. Herron, M. Mavrikakis, *Science* **2014**, *343*, 1339.
[184] Z. Wang, Y. Li, H. Yu, Y. Xu, H. Xue, X. Li, H. Wang, L. Wang, *ChemSusChem* **2018**, *11*, 3480.
[185] X.-L. Ma, J.-C. Liu, H. Xiao, J. Li, *J. Am. Chem. Soc.* **2018**, *140*, 46.
[186] P. Xiong, X. Zhang, H. Wan, S. Wang, Y. Zhao, J. Zhang, D. Zhou, W. Gao, R. Ma, T. Sasaki, *Nano Lett.* **2019**, *19*, 4518.
[187] Y.-T. Li, X.-L. Zhang, Z.-K. Peng, P. Liu, X.-C. Zheng, *Fuel* **2020**, *277*, 118243.
[188] D. Voiry, A. Mohite, M. Chhowalla, *Chem. Soc. Rev.* **2015**, *44*, 2702.
[189] Y. Yin, Y. Zhang, T. Gao, T. Yao, X. Zhang, J. Han, X. Wang, Z. Zhang, P. Xu, P. Zhang, *Adv. Mater.* **2017**, *29*, 1700311.
[190] Y. Gorlin, B. Lassalle-Kaiser, J. D. Benck, S. Gul, S. M. Webb, V. K. Yachandra, J. Yano, T. F. Jaramillo, *J. Am. Chem. Soc.* **2013**, *135*, 8525.
[191] P. Chen, K. Xu, S. Tao, T. Zhou, Y. Tong, H. Ding, L. Zhang, W. Chu, C. Wu, Y. Xie, *Adv. Mater.* **2016**, *28*, 7527.
[192] R. Liu, G. Xu, *Chin. J. Chem.* **2010**, *28*, 139.
[193] I. A. Amar, R. Lan, C. T. Petit, S. Tao, *J. Solid State Electrochem.* **2011**, *15*, 1845.
[194] S. Giddey, S. Badwal, A. Kulkarni, *Int. J. Hydrogen Energy* **2013**, *38*, 14576.
[195] V. Kyriakou, I. Garagounis, E. Vasileiou, A. Vourros, M. Stoukides, *Catal. Today* **2017**, *286*, 2.
[196] I. Garagounis, V. Kyriakou, A. Skodra, E. Vasileiou, M. Stoukides, *Front. Energy Res.* **2014**, *2*, 1.
[197] X. Cui, C. Tang, Q. Zhang, *Adv. Energy Mater.* **2018**, *8*, 1800369.
[198] J. Kong, A. Lim, C. Yoon, J. H. Jang, H. C. Ham, J. Han, S. Nam, D. Kim, Y.-E. Sung, J. Choi, *ACS Sustainable Chem. Eng.* **2017**, *5*, 10986.
[199] D. K. Yesudoss, G. Lee, S. Shanmugam, *Appl. Catal., B* **2021**, *287*, 119952.
[200] F. Köleli, T. Röpke, *Appl. Catal., B* **2006**, *62*, 306.
[201] F. Köleli, D. B. Kayan, *J. Electroanal. Chem.* **2010**, *638*, 119.
[202] K. Kim, N. Lee, C.-Y. Yoo, J.-N. Kim, H. C. Yoon, J.-I. Han, *J. Electrochem. Soc.* **2016**, *163*, F610.
[203] L. Hu, Z. Xing, X. Feng, *ACS Energy Lett.* **2020**, *5*,430.
[204] Y.-H. Xie, J.-D. Wang, R.-Q. Liu, X.-T. Su, Z.-P. Sun, Z.-J. Li, *Solid State Ionics* **2004**, *168*, 117.
[205] W. Wang, X. Cao, W. Gao, F. Zhang, H. Wang, G. Ma, *J. Membr. Sci.* **2010**, *360*, 397.
[206] R.-Q. Liu, Y.-H. Xie, J.-D. Wang, Z.-J. Li, B.-H. Wang, *Solid State Ionics* **2006**, *177*, 73.
[207] N. Cao, G. Zheng, *Nano Res.* **2018**, *11*, 2992.
[208] A. Sclafani, V. Augugliaro, M. Schiavello, *J. Electrochem. Soc.* **1983**, *130*, 734.
[209] G.-F. Chen, X. Cao, S. Wu, X. Zeng, L.-X. Ding, M. Zhu, H. Wang, *J. Am. Chem. Soc.* **2017**, *139*, 9771.
[210] I. Papai, A. Goursot, F. Fajula, D. Plee, J. Weber, *J. Phys. Chem.* **1995**, *99*, 12925.
[211] H. Mikosch, E. L. Uzunova, G. St. Nikolov, *J. Phys. Chem. B* **2005**, *109*, 11119.
[212] A. Yamamoto, K. Arashiba, S. Naniwa, K. Kato, H. Tanaka, K. Yoshizawa, Y. Nishibayashi, H. Yoshida, *Phys. Chem. Chem. Phys.* **2020**, *22*, 12368.
[213] Y. Qiao, P. Yuan, Y. Hu, J. Zhang, S. Mu, J. Zhou, H. Li, H. Xia, J. He, Q. Xu, *Adv. Mater.* **2018**, *30*, 1804504.
[214] S. Li, J. K. Lee, S. Zhou, M. Pasta, J. H. Warner, *Chem. Mater.* **2019**, *31*, 387.
[215] R. C. Hamme, S. R. Emerson, *Deep Sea Res., Part I* **2004**, *51*, 1517.
[216] N. Wang, W. Ma, Z. Ren, Y. Du, P. Xu, X. Han, *J. Mater. Chem. A* **2018**, *6*, 884.
[217] Z. Zhang, S. Wu, C. Yang, L. Zheng, D. Xu, R. Zha, L. Tang, K. Cao, X. g. Wang, Z. Zhou, *Angew. Chem., Int. Ed.* **2019**, *58*, 17782.
[218] X. G. Wang, Q. Zhang, X. Zhang, C. Wang, Z. Xie, Z. Zhou, *Small Methods* **2019**, *3*, 1800334.
[219] L. Li, C. Tang, X. Cui, Y. Zheng, X. Wang, H. Xu, S. Zhang, T. Shao, K. Davey, S. Z. Qiao, *Angew. Chem., Int. Ed.* **2021**, *133*, 14250.
[220] F. Abild-Pedersen, J. Greeley, F. Studt, J. Rossmeisl, T. R. Munter, P. G. Moses, E. Skulason, T. Bligaard, J. K. Nørskov, *Phys. Rev. Lett.* **2007**, *99*, 016105.
[221] T. Bligaard, J. K. Nørskov, S. Dahl, J. Matthiesen, C. H. Christensen, J. Sehested, *J. Catal.* **2004**, *224*, 206.
[222] J.-C. Liu, X.-L. Ma, Y. Li, Y.-G. Wang, H. Xiao, J. Li, *Nat. Commun.* **2018**, *9*, 1.
[223] D. Yao, C. Tang, L. Li, B. Xia, A. Vasileff, H. Jin, Y. Zhang, S. Z. Qiao, *Adv. Energy Mater.* **2020**, *10*, 2001289.
[224] S. Z. Andersen, V. Čolić, S. Yang, J. A. Schwalbe, A. C. Nielander, J. M. McEnaney, K. Enemark-Rasmussen, J. G. Baker, A. R. Singh, B. A. Rohr, *Nature* **2019**, *570*, 504.
[225] L. Li, C. Tang, D. Yao, Y. Zheng, S.-Z. Qiao, *ACS Energy Lett.* **2019**, *4*, 2111.
[226] R. Y. Hodgetts, A. S. Kiryutin, P. Nichols, H.-L. Du, J. M. Bakker, D. R. Macfarlane, A. N. Simonov, *ACS Energy Lett.* **2020**, *5*, 736.

Yang Li received her Ph.D. degree from Institute for Superconducting and Electronic Materials (ISEM), University of Wollongong (UOW), Australia in 2020 under the supervision of Prof. Shixue Dou. Then, she joined the group of Prof. Feng Pan at the School of Advanced Materials (SAM), Peking University, Shenzhen Graduate School, China, as a post-doctoral fellow from September 2020. Her research focuses on the synthesis and structure characterization of single-atom material for energy conversion and storage, including nitrogen reduction, carbon dioxide reduction, zinc–air batteries, and water splitting.

© 2021 Wiley-VCH GmbH

23669608, 2021, 11, Downloaded from https://onlinelibrary.wiley.com/doi/10.1002/smtd.202100460 by University Town Of Shenzhen, Wiley Online Library on [26/11/2025]. See the Terms and Conditions (https://onlinelibrary.wiley.com/terms-and-conditions) on Wiley Online Library for rules of use; OA articles are governed by the applicable Creative Commons License

Qi Zhang is an assistant research fellow with Engineering Research Center of Advanced Metal Composites Forming Technology and Equipment, Taiyuan University of Technology. He received his Bachelor and Ph.D. degree from Northeast Forestry University in 2013 and 2019. His current research interest is high value-added utilization of biomass, renewable energy storage, and conversion, including lithium/sodium ion batteries, lithium–sulfur batteries.

Zongwei Mei is currently an associate research fellow at School of Advanced Materials, Peking University, Shenzhen Graduate School, China. He received Ph.D. in Chemistry in 2013 from Hokkaido University, Japan. His research interests focus on the development, properties, and mechanism of photocatalytic/photoelectrochemical/electrocatalytic materials for water splitting and CO_2 reduction, and the catalyst for oxygen reduction reaction (ORR) and hydrogen oxidation reaction (HOR) in fuel cell.

Shunning Li received his B.E. degree in 2013 and Ph.D. degree in 2018 from School of Materials Science and Engineering, Tsinghua University, China. Currently, he is an associate research fellow at the School of Advanced Materials, Peking University, Shenzhen Graduate School, China. His research interest focuses on the first-principles design of energy storage materials and heterogeneous catalysts.

Wenbin Luo obtained his Ph.D. degrees from University of Wollongong, Australia. He is now professor at Northeastern University School of Metallurgy. His research has been focused on energy storage materials for battery applications, especially on electrocatalysts, metal–air batteries, and Li/Na-ion batteries.

© 2021 Wiley-VCH GmbH

23669608, 2021, 11, Downloaded from https://onlinelibrary.wiley.com/doi/10.1002/smtd.202100460 by University Town Of Shenzhen, Wiley Online Library on [26/11/2025]. See the Terms and Conditions (https://onlinelibrary.wiley.com/terms-and-conditions) on Wiley Online Library for rules of use; OA articles are governed by the applicable Creative Commons License

Feng Pan, chair professor, founding dean of School of Advanced Materials, Peking University, Shenzhen Graduate School, director of National Center of Electric Vehicle Power Battery and Materials for International Research, received his B.S. degree from the Department of Chemistry, Peking University in 1985 and Ph.D. from the Department of P&A Chemistry, University of Strathclyde, UK with ''Patrick D. Ritchie Prize'' for the best PhD in 1994. Prof. Pan has been engaged in fundamental research on structural chemistry, exploring ''Material Gene'' for Li-ion batteries, and developing novel energy conversion-storage materials and devices. He also received the 2018 ECS Battery Division Technology Award.

Huakun Liu is a distinguished professor and the founding program leader of energy materials at ISEM. She was awarded the Doctor of Science by the University of Wollongong in 2017. She is one of the Chief investigators for Auto CRC 2020 program on energy storage (2012–2017), aiming at achieving high energy density, high power density, safety and long cycle life lithium ion batteries for electric vehicles, and also for Smart Sodium Storage System project supported by Australian Renewable Energy Agency (ARENA, 2016–2020).

Shixue Dou is a distinguished professor at UOW, the founding director of ISEM and UOW Ambassador for Asia. He received his Ph.D. degree at Dalhousie University, Canada in 1984 and DSc at the University of New South Wales in 1998. He was awarded the Australian Government's Centenary Medal in 2003 and Australian Order of Member in 2019 for his contribution to materials science and engineering. His research focusses on energy materials for storage and conversion.

© 2021 Wiley-VCH GmbH

23669608, 2021, 11, Downloaded from https://onlinelibrary.wiley.com/doi/10.1002/smtd.202100460 by University Town Of Shenzhen, Wiley Online Library on [26/11/2025]. See the Terms and Conditions (https://onlinelibrary.wiley.com/terms-and-conditions) on Wiley Online Library for rules of use; OA articles are governed by the applicable Creative Commons License